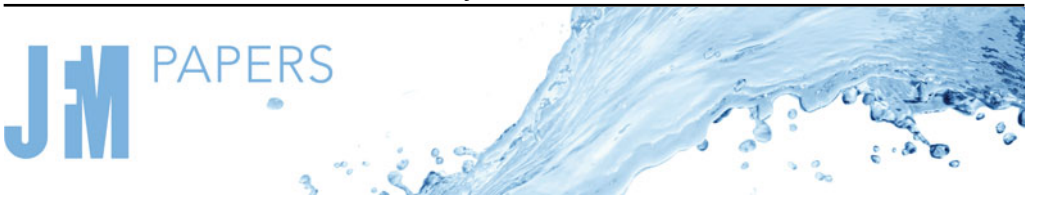
J. Fluid Mech. (2026), *vol.* 1027, A13, doi:10.1017/jfm.2025.11064



Atwood-number dependence of the instability evolution at a shock-accelerated heavy fluid layer

Chenren Chen[1], **Jiaxuan Li**[1] **and Zhigang Zhai**[1]

[1]State Key Laboratory of High-Temperature Gas Dynamics, School of Engineering Science, University of Science and Technology of China, Hefei 230026, PR China

Corresponding author: Zhigang Zhai, sanjing@ustc.edu.cn

(Received 4 August 2025; revised 1 December 2025; accepted 15 December 2025)

Numerical simulations and theoretical analysis are conducted to investigate the Atwood-number dependence of perturbation evolution in a shocked heavy fluid layer. For layers without reverberating waves, a higher Atwood number of one interface significantly enhances its coupling effect on the perturbation growth at the opposite interface. A theoretical model incorporating the startup, linear and nonlinear stages is developed to predict the interface mixing width. Dimensionless formulae are derived, identifying eight distinct modulation regimes of multi-interface instability. When reverberating waves are present, the individual effects of the upstream (A_1) and downstream (A_2) Atwood numbers are examined. The model is further modified to account for additional reverberating waves required at higher A_2 values for accurate amplitude prediction. Both theory and simulations demonstrate that perturbation growth at one interface can be actively controlled by adjusting the Atwood number of the opposite interface. These findings provide insights for mitigating instabilities in applications such as inertial confinement fusion through appropriate material selection.

Key words: shock waves

1. Introduction

Richtmyer–Meshkov instability (RMI) (Richtmyer 1960; Meshkov 1969) occurs when a shock wave impinges on a perturbed interface separating two different substances. This hydrodynamic instability has demonstrated critical importance in many applications (Ravid, Citron & Jeanloz 2021; Zhou 2024), such as inertial confinement fusion (ICF) (Betti & Hurricane 2016; Zylstra *et al.* 2022) and supernova explosions (Abarzhi *et al.* 2019). The baroclinic vorticity resulting from misalignment of the pressure and density gradients drives the RMI evolution (Hawley & Zabusky 1989; Jacobs *et al.* 1993). Over the past decades, extensive researches have yielded substantial advances in RMI

© The Author(s), 2026. Published by Cambridge University Press.

https://doi.org/10.1017/jfm.2025.11064 Published online by Cambridge University Press

understanding (Zabusky 1999; Brouillette 2002; Ranjan, Oakley & Bonazza 2011; Zhou 2017*a*, 2017*b*; Zhou *et al.* 2021, 2025*b*).

The perturbation evolution in RMI is predominantly governed by the interface parameters, such as the initial interface amplitude (Dell, Stellingwerf & Abarzhi 2015), interface wavelength (Haan 1991) and the specific heat ratios of the fluids (Vandenboomgaerde, Mügler & Gauthier 1998). Moreover, the interface Atwood number ($A = (\rho_d - \rho_u)/(\rho_d + \rho_u)$, where ρ_d and ρ_u denote the densities of substances downstream and upstream of the interface, respectively) has been demonstrated to significantly affect the RMI growth (Dimonte & Ramaprabhu 2010). Quantifying the influence of Atwood number on RMI evolution is critically important for practical applications. In ICF, RMI directly affects the target performance optimization (Kritcher *et al.* 2022) where different target designs employ ablator layers with different material densities, such as CH plastic versus high-density carbon (Lindl *et al.* 2014; Qiao & Lan 2021). Consequently, the Atwood number of key interfaces, particularly between the deuterium–tritium (DT) ice and ablator, or between successive ablative layers, varies significantly across ICF target configurations. An understanding of RMI's Atwood-number dependence is therefore essential for predicting performance and guiding the design of ICF targets.

For single-interface RMI with small initial amplitude, postshock perturbation evolution typically progresses through distinct stages. The perturbation growth rate first increases due to the startup process (Lombardini & Pullin 2009), and then enters the linear (Richtmyer 1960) and nonlinear stages (Zhang & Guo 2016). The Atwood number critically influences evolution across all stages. Analytical models for the startup process (Lombardini & Pullin 2009; Li *et al.* 2024*b*) revealed significant Atwood-number dependence in early amplitude evolution for both light–heavy (shock propagating from light to heavy fluids) and heavy–light (shock propagating from heavy to light fluids) configurations. In the linear stage, the classical impulsive model (Richtmyer 1960) quantified effect of Atwood number for light–heavy interfaces. Vandenboomgaerde *et al.* (1998) generalized this by developing an empirical model (VMG model) incorporating effects of both preshock and postshock Atwood numbers, making it applicable to all single-interface RMI scenarios. The modified impulsive model proposed by Velikovich, Herrmann & Abarzhi (2014) incorporates nonlinear corrections through a perturbation expansion method, improving predictions for initial bubble (light fluids penetrating to heavy fluids) and spike (heavy fluids penetrating to light fluids) growth rates in incompressible RMI while maintaining dependence on the Atwood number.

The above analytical models were developed under the incompressible approximation. When the compressibility effects become non-negligible in RMI flows, the reduced incompressible models like the impulsive model yield increasingly inaccurate predictions (Yang, Zhang & Sharp 1994; Mikaelian 1994; Velikovich *et al.* 2014). To address compressibility effects, Wouchuk & Nishihara (1996, 1997) derived analytical models (WN model) based on the compressible Euler equations, predicting linear RMI growth at both light–heavy and heavy–light interfaces. Wouchuk (2001*a*, 2001*b*) subsequently refined this model into a more compact form, optimizing the calculation of linear growth rates for compressible RMI. Further advancing this framework, Wouchuk & López Cavada (2004) investigated perturbation oscillations induced by acoustic waves emitted from perturbed shocks. For shock–interface interactions, Cobos Campos & Wouchuk (2016), Cobos-Campos & Wouchuk (2017) derived explicit analytical expansions for the asymptotic normal velocity of RMI growth by accounting for the complete history of acoustic perturbations between transmitted and reflected wavefronts. Most recently, Napieralski *et al.* (2024) proposed a fully compressible analytic theory capturing

https://doi.org/10.1017/jfm.2025.11064 Published online by Cambridge University Press

non-decaying perturbation oscillations. This theory provides an approximate formula applicable to fluids with arbitrary equations of state, predicting asymptotic RMI growth rates and thereby extending previous models limited to ideal equations of state. The Atwood number invariably dictates linear RMI growth rates across all these compressible theories.

As nonlinearity intensifies, high-order harmonics occurs at the shocked interface (Zhang & Sohn 1997). Crucially, Zhang & Sohn (1997) theoretically demonstrated a strong dependence of all harmonic amplitudes on Atwood number. Their work further quantified the growth of the spike and bubble to predict the interface mixing width. Subsequently, numerous analytical models have been developed to characterize spike/bubble evolution (Sadot *et al.* 1998; Mikaelian 2003; Dimonte & Ramaprabhu 2010; Nishihara *et al.* 2010; Zhang & Guo 2022; Zhou, Zhai & Luo 2025*b*). A universal feature of these models is the fundamental role of Atwood number as a governing parameter, explicitly embedded in the expressions describing nonlinear amplitude growth.

Numerically, Dimonte & Ramaprabhu (2010) revealed that the single-interface RMI evolution shows strong Atwood-number dependence, with spikes accelerating at high Atwood numbers due to the rapidly amplifying harmonics. Using vortex-based theory, Nishihara *et al.* (2010) analysed the distinct Atwood-number dependence patterns in planar versus cylindrical geometries. Thornber *et al.* (2010) investigated the effect of Atwood numbers on the power-law exponent of the RMI turbulent mixing width and found the distinct power-law under low- and high-Atwood-number conditions. Lombardini *et al.* (2011) considered a broad parameter space of initial Atwood number in simulations and found Atwood numbers strongly influence the turbulent kinetic energy, dissipation and postreshock mixing width growth. Experimentally, the foundational work by Meshkov (1969) established that the interface amplitude growth rate increases with Atwood numbers. While numerous experiments exploring RMI dynamics were within restricted ranges of Atwood numbers (Collins & Jacobs 2002; Niederhaus & Jacobs 2003; Mariani *et al.* 2008; Vandenboomgaerde *et al.* 2014; Mansoor *et al.* 2020; Li *et al.* 2024*a*), studies spanning a wide Atwood-number range (Motl *et al.* 2009; Chen *et al.* 2023), consistently confirm that the perturbation growth exhibits a pronounced correlation with Atwood numbers.

Richtmyer–Meshkov instability frequently occurs at multiple fluid interfaces in practical applications. In ICF capsules, for instance, RMI develops at multiple interfaces, including the ablative front (Qiao & Lan 2021), the interface between the ablator and DT ice (Amendt 2021), and the DT ice–gas interface (Lobatchev & Betti 2000). Thus, ignition-phase RMI in ICF typically involves a layered structure with multiple interfaces rather than a single one. Compared with RMI at a single interface, the RMI evolving at a multi-interface system is affected by more complex dynamics such as reverberating waves and interface-coupling effects. For RMI at a finite-thickness layer of heavy fluid, Jacobs *et al.* (1995) developed a linear model to quantify the interface-coupling effect, validating it with shock-tube experiments. Mikaelian (1996, 2005) investigated numerically and analytically the single-mode RMI evolution in both planar and cylindrical geometries for shocked layers. Theoretical analyses and numerical validations further demonstrated that RMI growth at such layers can be manipulated by modulating the initial interface morphology (Mikaelian 1996). Recent studies achieved stagnation of the downstream interface (DI) amplitude growth via modifying the upstream interface (UI) shape or the initial layer width (Sterbentz *et al.* 2022; Chen *et al.* 2024, 2025*a*). Cong *et al.* (2024) specifically isolated the interface-coupling mechanism by eliminating reverberating waves within the shocked heavy layer, designing conditions to stagnate perturbation growth at either UI or DI. However, for multi-interface RMI, while the effects of interface morphology and

https://doi.org/10.1017/jfm.2025.11064 Published online by Cambridge University Press

layer width have been extensively examined in prior studies, the range of Atwood numbers explored across these layer interfaces remains notably limited. While Yuan *et al.* (2024) numerically studied converging RMI at a cylindrical layer under varying Atwood numbers, their work prioritized validating an interface-coupling model, with discussion limited to the effect of DI Atwood number. Given the significant influence of Atwood numbers on RMI development, a thorough understanding of their impact on both the evolution of RMI and the modulation mechanisms of perturbations at a shocked layer is essential.

In summary, existing studies primarily focused on the effects of the initial shape or layer width on the RMI evolution at a shocked fluid layer. Alternatively, some works examined the influence of a wide range of Atwood numbers on the RMI evolution at a single shocked interface. However, the effect of a broad range of Atwood numbers on the evolution of a shocked layer has been rarely addressed. Across distinct Atwood-number conditions, how does interface coupling affect the RMI evolution? How can theoretical models quantify the respective effects of Atwood number of each interface on perturbation growth when both reverberating waves and interface coupling are present? Is it possible to selectively control RMI growth at UI by adjusting the Atwood number of DI, and *vice versa*? To address these questions, this study systematically investigates the dependence of RMI evolution on the Atwood number in a heavy fluid layer. First, following an approach similar to that of Cong *et al.* (2024), we eliminate reverberating waves within the layer to isolate the role of the Atwood number in pure interface coupling. Second, by systematically varying the Atwood numbers to modify interface-coupling effects, we explore strategies for modulating RMI in a layer that satisfies the total-transmission condition. Third, we simulate the amplitude evolution of both the UI and DI under a range of Atwood numbers, incorporating the full influence of reverberating waves. Based on these results, we develop theoretical models to quantitatively describe how multi-interface RMI evolution depends on the Atwood numbers. Finally, with the effects of reverberating waves taken into account, we demonstrate targeted control of perturbation growth at the UI (or DI) by strategically adjusting the Atwood number of the DI (or UI).

2. Numerical methods

2.1. *Numerical set-up and scheme*

This work employs numerical simulations to resolve the shocked flow features and elucidate their Atwood-number dependence. The initial computational domain is shown in figure 1(*a*). The incident shock (IS) is positioned 10 mm upstream of the UI, and the distance between the average UI and DI positions is defined as L_0. The system contains three gaseous media: gas 1 (upstream of the layer), gas 2 (inside the layer) and gas 3 (downstream of the layer); and gas 2 has a higher density than gases 1 and 3. Identical single-mode perturbations with wavelength λ are imposed on both the UI and DI. The computational domain spans 250 mm in the x-direction, while its width in the y-direction equals λ. Open boundary conditions are applied at the left- and right-hand boundaries, and periodic boundary conditions are used at the upper and lower boundaries. Computational efficiency is optimized by restricting calculations to a 200 mm extent along the orthogonal axes. All simulations are performed at an initial temperature of 297.8 K and pressure of 101.3 kPa. Detailed numerical settings, including the IS Mach number (M_{IS}), initial UI and DI amplitudes (a_{1-} and a_{2-}), and initial densities of the three gaseous media (ρ_{10}, ρ_{20}, ρ_{30}), are presented in §§ 3–5.

The interaction between the shock and the fluid layer is governed by the two-dimensional multicomponent non-reactive Euler equations, expressed in conservative form as detailed in our prior numerical framework (Chen *et al.* 2025*b*). Simulations employ the high-order

https://doi.org/10.1017/jfm.2025.11064 Published online by Cambridge University Press

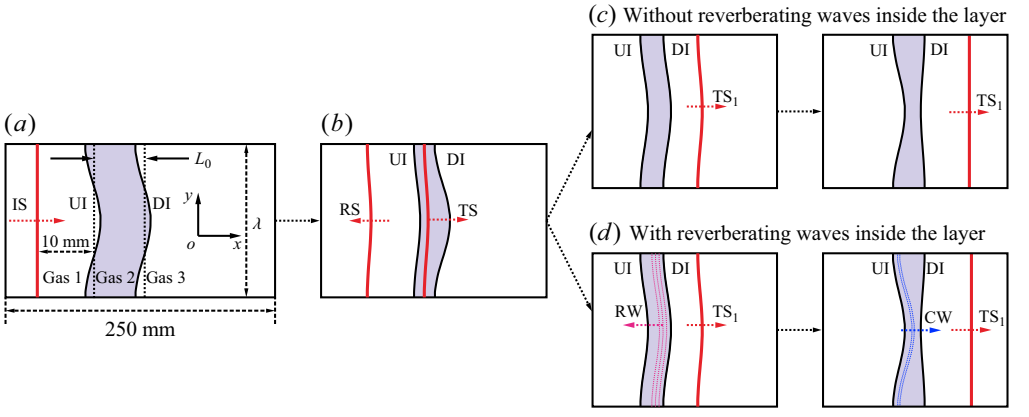


Figure 1. Schematics of (*a*) the initial computational domain for a planar shock interacting with a heavy layer with two single-mode interfaces, (*b*) the generation of the transmitted shock (TS) inside the layer and the reflected shock (RS), (*c*) the flow evolution after a shock passes through a layer without reverberating waves and (*d*) the generation of the reverberating waves within a shocked heavy layer. Here, λ and L_0 denote the perturbation wavelength and the initial layer width, respectively; IS denotes the incident shock; UI and DI represent the upstream and downstream interface of the layer, respectively; TS and RS denote the transmitted shock inside the layer and reflected shock generated by IS impacting UI, respectively; TS_1 denotes the transmitted shock moving away from the layer; RW and CW denote the rarefaction waves and compression waves within the shocked layer, respectively.

weighted essentially non-oscillatory (WENO) and double flux (HOWD) scheme (Ding *et al.* 2017). This method combines a fifth-order WENO reconstruction (Jiang & Shu 1996) with the double flux algorithm (Abgrall & Karni 2001; Billet & Abgrall 2003) to accurately capture material interfaces and wave patterns. Time integration uses a third-order total variation diminishing Runge–Kutta scheme. The HOWD scheme has proven effective for simulating RMI at both single interfaces and layers (Li *et al.* 2024*b*; Cao *et al.* 2024). Further implementation details are available in Ding *et al.* (2017).

2.2. *Evaluation of grid convergence and code validation*

To establish mesh independence, four grid sizes (0.4, 0.2, 0.1 and 0.05 mm) are tested for a heavy fluid layer configuration with $\lambda = 40$ mm, $L_0 = 10$ mm and dimensionless perturbation amplitudes $ka_{1-} = ka_{2-} = 0.1$ ($k = 2\pi/\lambda$ denotes the perturbation wavenumber), under $M_{IS} = 1.20$ shock loading. The gas composition is 31.1 % xenon/68.9 % helium for gases 1 and 3, and 100 % xenon for gas 2. This yields postshock Atwood numbers of $A_1 = 0.5$ at the UI and $A_2 = -0.5$ at the DI. Notably, the compositions of specific gases in fluids 1, 2 and 3 do not evolve, demonstrating that after fixing the compositions in one case, the Atwood number is only varied by changing the density of the specific gas. Interfaces are operationally defined where the gas 2 volume fraction equals 50 %. The mixing width (w) is the x-direction distance between the interface nodes with the maximum and minimum x. Temporal initialization ($t = 0$) corresponds to IS reaching the UI's average position. Figure 2(*a*) shows the temporal evolution of w for the UI and DI across mesh resolutions. Convergence is observed for both interfaces at 0.10 and 0.05 mm resolutions. We therefore adopt 0.10 mm to balance computational cost and accuracy.

For code validation, numerical results using the 0.1 mm mesh are benchmarked against experimental mixing width data from a shocked air/SF_6/air layer (Li *et al.* 2023), as shown in figure 2(*b*). The computational set-up replicates the experimental initial conditions: $M_{IS} = 1.19$, $\lambda = 60$ mm, $L_0 = 49$ mm, $a_{1-} = 0$ mm and $a_{2-} = 4$ mm, with

https://doi.org/10.1017/jfm.2025.11064 Published online by Cambridge University Press

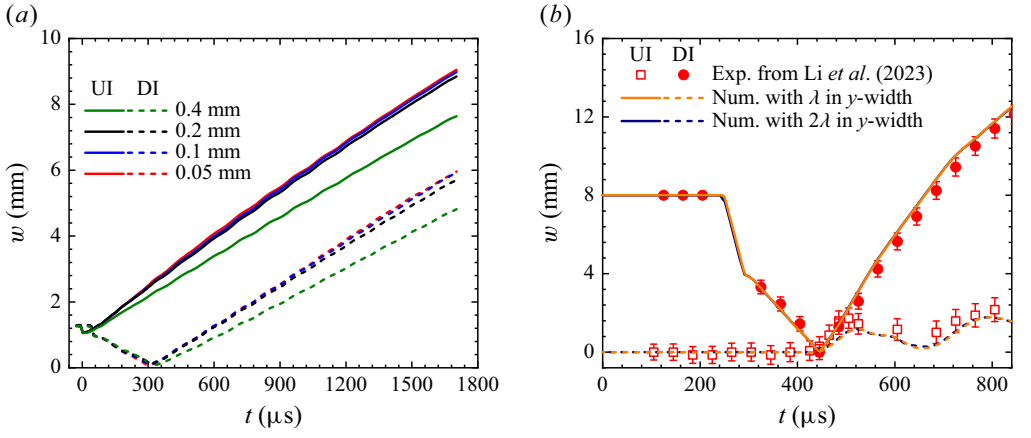


Figure 2. Code validation. (*a*) Grid convergence verification through comparing the interface mixing width of a shocked helium/xenon/helium layer, and (*b*) comparison of the interface mixing width of a shocked air/SF_6/air layer between the experiments (Li *et al.* 2023) and 0.1-mesh-size numerical simulations using the domains with y-direction width equal to λ and 2λ.

82.6 % SF_6 in the layer and pure air externally. Quantitative agreement is observed between the results from the simulation and the previous experiment. Note that the one-wavelength transverse extent of the numerical domain has the potential to restrict the growth of perturbations with wavelengths exceeding that of the fundamental mode. However, in this work, only the overall mixing width of the interface, the amplitude of the fundamental mode and the amplitudes of high-order modes with wavelengths shorter than the fundamental wavelength are extracted from the simulations and analysed. Modes with wavelengths longer than the transverse domain size are not considered in either the numerical or theoretical analysis. To verify that the one-wavelength transverse extent does not significantly affect the evolution of the interface mixing width, an additional simulation is performed using a domain with a two-wavelength transverse extent. A comparison of the results obtained from the one-wavelength and two-wavelength domains is provided in figure 2(*b*). The close agreement between these results confirms that the one-wavelength transverse extent has a negligible influence on the development of the interface mixing width.

3. Result and discussion

The influence of the Atwood numbers on the evolution and modulation of RMI at a layer is examined in the following four subsections, categorized by the satisfaction of the total-transmission condition. The evolution of RMI in a fluid layer is simultaneously influenced by a complex set of parameters. These include the Atwood numbers of both the upstream (A_1) and downstream (A_2) interfaces, the IS Mach number, the adiabatic indices of the fluids, the layer width and the initial interface geometry. To decouple the specific effects of A_1 and A_2, we designed a series of distinct shock-layer configurations. The numerical cases conducted in different subsections are labelled through A_1 and A_2, as detailed in table 1. Note that the layer width influences the duration of the linear stage of RMI in a shocked layer. A decrease in layer width can lead to the rapid collision of RMI-induced fingers at the two interfaces, thereby accelerating the onset of nonlinear mixing. In this study, the theoretical model is derived using the potential function method, which loses validity once the two interfaces collide. As a result, layers with particularly narrow widths

https://doi.org/10.1017/jfm.2025.11064 Published online by Cambridge University Press

Layer conditions	Analysis subsection	Case	A_1	A_2
Total-transmission condition	§ 3.1	TT/0.10/−0.50	0.10	−0.50
		TT/0.30/−0.50	0.30	−0.50
		TT/0.50/−0.50	0.50	−0.50
		TT/0.70/−0.50	0.70	−0.50
		TT/0.90/−0.50	0.90	−0.50
Total-transmission condition	§ 3.2	MT/0.50/−0.50	0.50	−0.50
		MT/0.13/−0.50	0.13	−0.50
		MT/−0.30/−0.50	−0.30	−0.50
		MT/−0.62/0.20	−0.62	0.20
		MT/−0.50/0.50	−0.50	0.50
		MT/−0.11/0.50	−0.11	0.50
		MT/0.50/0.50	0.50	0.50
		MT/0.64/−0.30	0.64	−0.30
		MT-AP/0.14/0.50	0.14	0.50
		MT-AP/−0.57/−0.30	−0.57	−0.30
Non-total-transmission condition	§ 3.3	0.10/−0.50	0.10	−0.50
		0.50/−0.10	0.50	−0.10
		0.50/−0.50	0.50	−0.50
		0.50/−0.90	0.50	−0.90
		0.90/−0.50	0.90	−0.50
Non-total-transmission condition	§ 3.4	M/0.30/−0.30	0.30	−0.30
		M/0.50/−0.30	0.50	−0.30
		M/0.70/−0.30	0.70	−0.30
		M2/0.30/−0.30	0.30	−0.30
		M2/0.30/−0.50	0.30	−0.50
		M2/0.30/−0.70	0.30	−0.70

Table 1. Overview of the numerical cases run in § 3, listing the transmission condition of the layer, the subsections in which the simulations are analysed, the names of the cases and the Atwood numbers of UI (A_1) and DI (A_2) in each case.

are not considered here. The primary quantities in the theoretical analysis are clearly defined by their physical meanings in table 2. All derived models assume single-mode perturbation dominance at the interfaces and incompressible flow.

3.1. *Atwood-number dependence under total-transmission condition*

When the IS interacts with the UI, it generates a TS inside the layer and RS that propagates back into the upstream gas, as shown in figure 1(*b*). To isolate the interface-coupling effect on multi-interface RMI, reverberating waves within the layer should be eliminated. This elimination occurs when a shock passes through a gas interface satisfying the total transmission condition, a relationship between the shock Mach number and the thermophysical properties of the adjacent gases (Han & Yin 1993). The total transmission condition for the DI is given by

$$\frac{1+A_2}{1-A_2}=\frac{\gamma_2(\gamma_2+1)M_{TS}^2}{\gamma_3-\gamma_2+\gamma_2(\gamma_3+1)M_{TS}^2}, \tag{3.1}$$

where M_{TS} denotes the Mach number of TS, while γ_2 and γ_3 represent the adiabatic indices for gas 2 and gas 3, respectively. Equation (3.1) has been numerically validated for accuracy and reliability in prior work (Cong *et al.* 2024). Figure 1(*a–c*) schematically

https://doi.org/10.1017/jfm.2025.11064 Published online by Cambridge University Press

Notation	Physical meaning
A_1	Atwood number of shocked UI
A_2	Atwood number of shocked DI
M_{IS}	Mach number of IS
M_{TS}	Mach number of TS inside the layer
k	Wavenumber of the perturbation
L_0	Width of the initial layer
L	Width of the layer just after it is shocked
a_{1-}	Amplitude of initial UI
a_{1+}	Amplitude of shocked UI
a_{2-}	Amplitude of initial DI
a_{2+}	Amplitude of shocked DI
a_{1R}	Amplitude of UI being impacted by rarefaction waves
a_{2C}	Amplitude of DI being impacted by CW
a_s	Amplitude of TS inside the layer
a_R	Amplitude of rarefaction waves inside the layer
a_C	Amplitude of CW inside the layer
v_{IS}	Velocity of IS
v_1^t	Velocity of TS inside the layer
v_1^f	Velocity of RS
Δu_1	Jump velocity of UI induced by IS
Δu_2	Jump velocity of DI induced by TS
Δu_R	Jump velocity of UI induced by rarefaction waves
Δu_C	Jump velocity of DI induced by CW
c_1	Sound speed in the gas behind TS inside the layer
c_2	Sound speed in the gas behind rarefaction waves inside the layer
t_1^c	Duration of shock compressing UI
t_1^{st}	Duration of startup process at UI
t_2^c	Duration of shock compressing DI
t_2^{st}	Duration of startup process at DI
t_1	Instant of the TS impacting DI
t_2	Instant of the first rarefaction waves impacting UI
t_3	Instant of the first CW impacting DI

Table 2. Summary of notations representing the primary physical parameters in this work.

illustrate the shock-layer interaction during total transmission at the DI. Under this condition, TS traverses the DI without generating a reflecting rarefaction wave (RW), producing only a TS_1 that propagates through gas 3. This absence of RW precludes secondary reverberating waves within the layer.

In this subsection, for the total-transmission condition without reverberating waves, if A_2 is changed, the adiabatic indices of the fluids within and downstream the layer must be significantly adjusted to satisfy (3.1). Therefore, only A_1 is changed in this part to investigate the Atwood-number dependence of multi-interface RMI under total-transmission condition. To isolate the effect of A_1, the adiabatic indices of all fluids, as well as the densities of the fluids within and downstream the layer, are held constant across all numerical cases. The initial perturbations for both interfaces are held constant, with a scaled amplitude (ka) of 0.1 and a wavelength (λ) of 40 mm. Meanwhile, the initial layer width is fixed at 10 mm. The initial upstream fluid density (ρ_{10}) is systematically adjusted to achieve different A_1 values. Critically, to maintain a consistent compression effect on the DI, the IS strength is calibrated in each case to ensure a constant Mach number for the TS within the layer. Consequently, both the initial and postshock parameters of the DI remain fixed. Under the total-transmission condition, this also results in a fixed jump

https://doi.org/10.1017/jfm.2025.11064 Published online by Cambridge University Press

Case	A_1	A_2	ρ_{10}	ρ_{20}	ρ_{30}	γ_1	γ_2	γ_3	M_{IS}
TT/0.10/−0.50	0.10	−0.50	4.878	5.976	2.864	1.094	1.094	2.641	1.372
TT/0.30/−0.50	0.30	−0.50	3.191	5.976	2.864	1.094	1.094	2.641	1.334
TT/0.50/−0.50	0.50	−0.50	1.964	5.976	2.864	1.094	1.094	2.641	1.300
TT/0.70/−0.50	0.70	−0.50	1.064	5.976	2.864	1.094	1.094	2.641	1.267
TT/0.90/−0.50	0.90	−0.50	0.327	5.976	2.864	1.094	1.094	2.641	1.228

Table 3. Initial conditions of numerical cases in which the total transmission condition is imposed at the DI. Here A_1 (A_2) denotes the Atwood number of the shocked UI (DI); ρ_{10} (γ_1), ρ_{20} (γ_2) and ρ_{30} (γ_3) denote the initial densities (adiabatic exponents) of gases 1, 2 and 3, respectively; M_{IS} denotes the IS Mach number. The unit of density is kg m^{-3}.

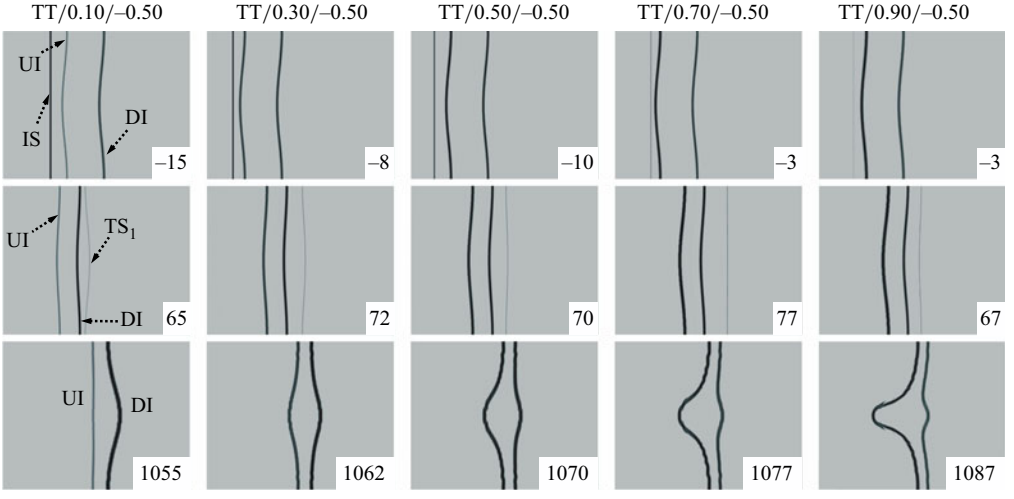


Figure 3. Numerical schlieren images for the evolution of a shocked heavy layer without reverberating waves. The symbols have the same meaning as those in figure 1. Numbers in the schlieren images denote time with unit of μs.

velocity, which is equal for both the UI and DI. Initial conditions of numerical cases in this subsection are provided in table 3. The Mach number of TS within the layer ($M_{TS} = 1.394$) is prescribed and combined with fixed γ_2 and γ_3 to satisfy (3.1). For this configuration, $\gamma_1 = \gamma_2$, while M_{IS} is derived from one-dimensional gas theory using $M_{TS} = 1.394$.

Figure 3 presents numerical schlieren images of shocked-layer morphology for the five reverberation-free cases. Time origin is defined as the moment when IS reaches the UI average position. Using case TT/0.10/−0.50 as an example, upon TS impacting the DI, a downstream-propagating TS_1 forms in gas 3, and reverberating waves are absent within the layer (65 μs). The late-stage evolution (1055 μs) shows substantial morphological divergence at both UI and DI under different A_1 conditions. For the UI, its amplitude is amplified with stronger bubble/spike development at higher A_1, which is analogous to single-interface RMI evolution (Chen *et al.* 2023). When $A_1 = 0.1$, progressive attenuation and phase inversion (the positions of the spike and bubble at the interface have been swapped) occur for the UI perturbation (the phase of preshocked UI and DI is defined as positive hereafter). For the DI, the perturbation generally undergoes a phase reversal for cases with $A_1 \leqslant 0.5$. In the case of TT/0.70/−0.50, the DI morphology transitions from single-mode to multimode. Notably in the case of TT/0.90/−0.50, the DI shows

https://doi.org/10.1017/jfm.2025.11064 Published online by Cambridge University Press

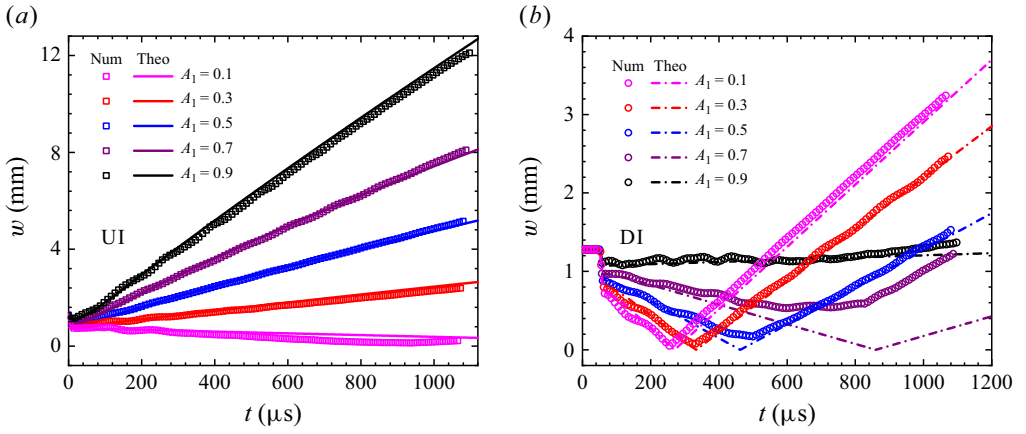


Figure 4. Comparison of the mixing width of UI (*a*) and DI (*b*) between numerical simulations and theoretical predictions for a shocked layer without reverberating waves.

suppression of phase reversal with spike structures at the bubble tip. In general, in low A_1 scenarios, the DI evolution governs the flow, whereas in high A_1 scenarios, the UI growth dominates.

The temporal evolution of mixing widths for the UI and DI are plotted in figure 4(*a*) and 4(*b*), respectively. The enhanced growth rate of the UI perturbation at higher A_1 and the complete phase reversal of the UI at $A_1 = 0.1$ are both clearly observed. The DI morphology at $A_1 = 0.7$ undergoes an incomplete phase-inversion process (non-recovery of planar geometry), and near-stagnation of the DI mixing width at $A_1 = 0.9$ is achieved due to UI coupling. These results demonstrate strategic RMI modulation feasibility through A_1 control.

To predict the RMI evolution when interface coupling is involved, the four stages of single-mode perturbation development at a shocked single interface is referenced (Zhai *et al.* 2025). In the shock compression stage, the UI amplitude can be expressed as

$$a_1(t) = a_{1-} - \frac{\Delta u_1}{2}\left(t + \frac{a_{1-}}{v_{IS}}\right) \qquad (-t_1^c \leqslant t \leqslant t_1^c), \tag{3.2}$$

where Δu_1 denotes the jump velocity of the UI induced by IS, v_{IS} denotes the IS velocity and $t_1^c = a_{1-}/v_{IS}$ represents the duration when compression of the UI is finished. After the compression stage, the startup process occurs (Lombardini & Pullin 2009) and its duration for the perturbation at the UI can be expressed as

$$t_1^{st} = \frac{1}{k}\left(\frac{1 - A_1}{v_1^f + \Delta u_1} + \frac{1 + A_1}{v_1^t - \Delta u_1}\right), \tag{3.3}$$

where v_1^f is the velocity of RS induced by IS striking with the UI. For the light–heavy RMI, the amplitude growth in the startup period was quantified by Lombardini & Pullin (2009) as

$$\dot{a}_1(t) = \frac{2\dot{a}_1^{lin}}{(1 + A_1)\coth(kL_{T1}) + (1 - A_1)\coth(kL_{F1})} \qquad (t_1^c < t \leqslant t_1^c + t_1^{st}), \tag{3.4}$$

where

$$L_{T1} = (v_1^t - \Delta u_1)(t - t_1^c) \quad \text{and} \quad L_{F1} = (v_1^f + \Delta u_1)(t - t_1^c) \tag{3.5}$$

https://doi.org/10.1017/jfm.2025.11064 Published online by Cambridge University Press

are the displacements of TS and RS, respectively, and $\dot{a}_1^{lin}$ is the linear growth rate of the UI amplitude. In this work, since the gases 1, 2 and 3 are different, the linear growth rates of both the UI amplitude and the DI amplitude ($\dot{a}_2^{lin}$) can be solved based on the model proposed in our previous work (Chen *et al.* 2025*b*):

$$\begin{aligned}&\dot{a}_1^{lin}[\rho_{1+}+\rho_{2+}\tanh(kL/2)]+\dot{a}_2^{lin}[\rho_{3+}+\rho_{2+}\tanh(kL/2)]\\&\quad=k\Delta u_1(\rho_{2+}-\rho_{1+})a_{1+}+k\Delta u_2[(\rho_{30}-\rho_{20})a_{2-}+(\rho_{3+}-\rho_{2+})a_{2+}]/2,\end{aligned}\tag{3.6}$$

$$\begin{aligned}&\dot{a}_1^{lin}[\rho_{1+}+\rho_{2+}\coth(kL/2)]-\dot{a}_2^{lin}[\rho_{3+}+\rho_{2+}\coth(kL/2)]\\&\quad=k\Delta u_1(\rho_{2+}-\rho_{1+})a_{1+}-k\Delta u_2[(\rho_{30}-\rho_{20})a_{2-}+(\rho_{3+}-\rho_{2+})a_{2+}]/2.\end{aligned}\tag{3.7}$$

Here, $L=L_0(1-\Delta u_1/v_1^t)$ is the layer width when TS passes through the DI and Δu_2 is the jump velocity of the DI induced by TS. According to the impulsive model (Richtmyer 1960) and the VMG model (Vandenboomgaerde *et al.* 1998), ρ_{1+}, ρ_{2+} and ρ_{3+} are the densities of shocked gases 1, 2 and 3, respectively. Here $a_{1+}=a_{1-}(1-\Delta u_1/v_{IS})$ is the initial shocked amplitude of the UI, and a_{2+} is the DI amplitude immediately after TS acceleration, which will be derived subsequently. Notably, the above models are applicable for perturbations with small initial amplitudes. For $t>t_1^c+t_1^{st}$ (marking UI's transition to nonlinear evolution), we adopt the mSEA model (Sadot *et al.* 1998; Xing *et al.* 2025), originally developed for single-interface RMI, to quantify the nonlinear behaviour of a_1. The mSEA formulation is

$$\begin{cases}\dot{a}_1(t)=(\dot{a}_{1b}(t)+\dot{a}_{1s}(t))/2 & (t>t_1^c+t_1^{st}),\\ \dot{a}_{1b/s}(t)=\dot{a}_1^{lin}\dfrac{1+k\dot{a}_1^{lin}(t-t_1^c-t_1^{st})}{1+(1\pm A_1)k\dot{a}_1^{lin}(t-t_1^c-t_1^{st})+F_{b/s}[k\dot{a}_1^{lin}(t-t_1^c-t_1^{st})]^2},\end{cases}\tag{3.8}$$

where $F_{b/s}=3(1\pm A_1)/(2+2A_1)$ when $A_1\geqslant 0.5$ and $F_{b/s}=(1\pm A_1)/(1+A_1)$ when $A_1<0.5$. Combining models (3.2)–(3.8), the mixing width of the shocked UI can be theoretically predicted ($w_1(t)=2a_1(t)$), as shown in figure 4(*a*) by lines. Good agreement between theoretical predictions and the numerical results validates the efficacy of (3.6)–(3.7) in quantifying the interface-coupling effect across diverse Atwood numbers. This agreement confirms that single-interface models (Chen *et al.* 2023; Xing *et al.* 2025) successfully capture the UI's nonlinear evolution in multi-interface systems.

The DI amplitude derivation (a_2) accounts for TS distortion effects absent in a_1 calculations. When IS traverses UI, the TS amplitude can be expressed as

$$a_{s0}=a_{1-}\left(1-\frac{v_1^t}{v_{IS}}\right).\tag{3.9}$$

At $t_1=L_0/v_1^t$, TS reaches DI's average position with amplitude (a_{s1}) being calculated by the model ((58) deduced by Bates (2004)). The DI compression lasts $2t_2^c=2(a_{2-}-a_{s1})/v_1^t$, yielding amplitude evolution

$$a_2(t)=a_{2-}-\frac{\Delta u_2}{2}\left(t-t_1+\frac{a_{2-}-a_{s1}}{v_1^t}\right)\qquad(t_1-t_2^c\leqslant t\leqslant t_1+t_2^c).\tag{3.10}$$

Based on (3.10), the DI amplitude just after TS acceleration is expressed as $a_{2+}=a_{2-}-\Delta u_2/v_1^t(a_{2-}-a_{s1})$, which can be substituted into (3.6)–(3.7). After TS passes through the DI, the duration of startup process of the DI can be calculated by the Li-model

https://doi.org/10.1017/jfm.2025.11064 Published online by Cambridge University Press

(Li *et al.* 2024*b*),

$$t_2^{st} = \frac{1}{k}\left(\frac{1-A_2}{c_1+c_2+\Delta u_2-\Delta u_1}+\frac{1+A_2}{v_2^t-\Delta u_2}\right), \tag{3.11}$$

where v_2^t denotes TS_1 velocity in gas 3. Here c_1 and c_2 denote the sound speeds in gas 2 between the UI and TS, and between the DI and RW tail, respectively. Here, $c_2 = c_1$ due to RW elimination. Based on the work of Li *et al.* (2024*b*), the DI growth during startup period is

$$\dot{a}_2(t) = \frac{2\dot{a}_2^{lin}}{(1+A_2)\coth(kL_{T2})+(1-A_2)\coth(kL_{F2})} \qquad (t_1+t_2^c < t \leqslant t_1+t_2^c+t_2^{st}), \tag{3.12}$$

where

$$L_{T2} = (v_2^t-\Delta u_2)(t-t_1-t_2^c) \quad \text{and} \quad L_{F2} = (c_1+c_2+\Delta u_2-\Delta u_1)(t-t_1-t_2^c)/2 \tag{3.13}$$

represent the displacements of TS_2 and RW, respectively, and $\dot{a}_2^{lin}$ is the linear growth rate of the DI amplitude derived from (3.6)–(3.7). After the startup process, DI's nonlinearity is neglected due to small mixing width, as shown in figure 4(*b*). Actually, the mixing width of the DI is much smaller than that of the UI in cases only with large Atwood number of the UI ($A_1 \geqslant 0.5$). For cases with $A_1 = 0.3$ and $A_1 = 0.1$, the widths of both the UI and DI are comparable, but both them are small ($kw/2 < 0.3$), and thus nonlinearity has very limited effects on the width evolution of both the UI and DI, as suggested by Mikaelian (2003). As a result, the linear growth rate can quantify the amplitude evolution of the DI,

$$\dot{a}_2(t) = \dot{a}_2^{lin} \qquad (t > t_1+t_2^c+t_2^{st}). \tag{3.14}$$

The theoretical DI mixing widths ($w_2 = 2a_2$) calculated from (3.9)–(3.14) are presented by lines in figure 4(*b*). These models effectively quantify interface-coupling effects on single-mode DI perturbations across A_1 values, with deviation only in the case with $A_1 = 0.70$.

To reveal the origin of theory–simulation discrepancies in the case with $A_1 = 0.7$, systematic modal decomposition of the DI perturbations is conducted and compared for cases TT/0.10/−0.50, TT/0.70/−0.50 and TT/0.90/−0.50. The fast Fourier transform (FFT) analysis of the first three harmonic modes are conducted and the temporal ratio of amplitudes of higher-order harmonics (modes 2–3) to the amplitude of basic mode a_{basic} are plotted in figure 5(*a*). In the case of $A_1 = 0.1$, higher-order harmonics (modes 2–3) remain negligible, confirming the DI mixing width is governed by the fundamental mode and well-predicted by (3.9)–(3.14). A notable contrast in the relative magnitudes between the fundamental mode and high-order harmonics is observed for $A_1 = 0.7$ and 0.9. In the case of $A_1 = 0.9$, the fundamental mode remains significantly larger in amplitude than the second and third harmonics until $t = 700$ μs. By $t = 1000$ μs, however, the amplitudes of the high-order harmonics become comparable to that of the fundamental mode. As a result, theoretical predictions agree well with numerical results up to $t = 700$ μs, but begin to deviate slightly by $t = 1000$ μs. In contrast, for $A_1 = 0.7$, the amplitude of the fundamental mode decreases more rapidly, allowing the growing second harmonic to surpass it around $t = 700$ μs. When considering both the second and third harmonics, high-order modes significantly exceed the fundamental mode, indicating that the interface distortion is dominated by high-order harmonics. Consequently, models based solely on

https://doi.org/10.1017/jfm.2025.11064 Published online by Cambridge University Press

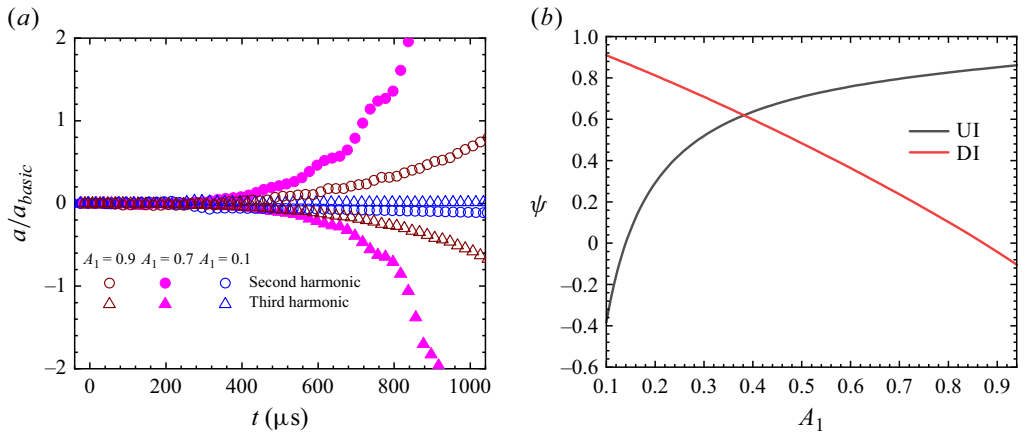


Figure 5. (*a*) The temporal ratios of harmonic modes amplitudes of DI to the basic mode amplitude a_{basic} at DI for cases with $A_1 = 0.9$, 0.7 and 0.1; (*b*) the ratio between perturbation growth rate of the layer interfaces and the growth rate of a shocked single interface (ψ) versus the Atwood number of the UI.

the fundamental mode begin to deviate from the numerical results at an earlier stage in the $A_1 = 0.7$ case.

To investigate the A-dependence of interface coupling, we introduce a normalized parameter ψ defined as the ratio between linear amplitude growth rates of the layer interfaces calculated by (3.6) and those of shocked single interfaces calculated by the impulsive model (Richtmyer 1960) for the UI and the VMG model (Vandenboomgaerde *et al.* 1998) for the DI. The dimensionless quantity ψ of the UI (ψ_1) and the DI (ψ_2) are formulated as

$$\begin{cases} \psi_1 = \dot{a}_1^{lin}/(ka_{1+}A_1\Delta u_1), \\ \psi_2 = \dot{a}_2^{lin}/[k\Delta u_2(a_{2+}A_2 + a_{2-}A_{20})/2], \end{cases} \tag{3.15}$$

where $A_{20} = (\rho_{30} - \rho_{20})/(\rho_{30} + \rho_{20})$ is the Atwood number of the DI prior to shock passage.

The calculated ψ of the two interfaces versus A_1 is presented in figure 5(*b*). The absolute values of both ψ_1 and ψ_2 remain universally below 1 across A_1 variations, demonstrating that the interface coupling suppresses the amplitude growth for both the UI and DI in this work. With A_1 increasing from 0.1 to 0.9, the interface-coupling effects for the two interfaces exhibit monotonic dependence on A_1. For the light–heavy perturbation at the UI, its growth exhibits phase reversal at low A_1 (approximately $A_1 < 0.15$) due to interface coupling relative to the perturbation in the single-interface condition. As A_1 decreases, the term $ka_{1+}A_1\Delta u_1$ decreases in magnitude. This leads to a more sensitive variation in ψ_1 as A_1 changes, primarily by modulating $\dot{a}_1^{lin}$. When A_1 becomes sufficiently small, the intrinsic perturbation growth at a single UI becomes negligible. In this regime, the coupling between interfaces dominates over the perturbation growth at UI. At high A_1, the UI amplitude growth rate asymptotically approaches the rate in the single-interface condition. For the heavy–light perturbation at the DI, its growth closely approximates the single-interface condition at low A_1, which means that the DI morphology is dominated by the fundamental harmonic. As A_1 increases, the decreasing ψ_2 indicates that the basic mode decays in the early stage with a suppressing rate compared with the single-interface condition, leading to the DI morphology being dominated by the high-order harmonics soon. Under high A_1 (approximately $A_1 > 0.87$) conditions, $\psi_2 < 0$, the interface coupling

https://doi.org/10.1017/jfm.2025.11064 Published online by Cambridge University Press

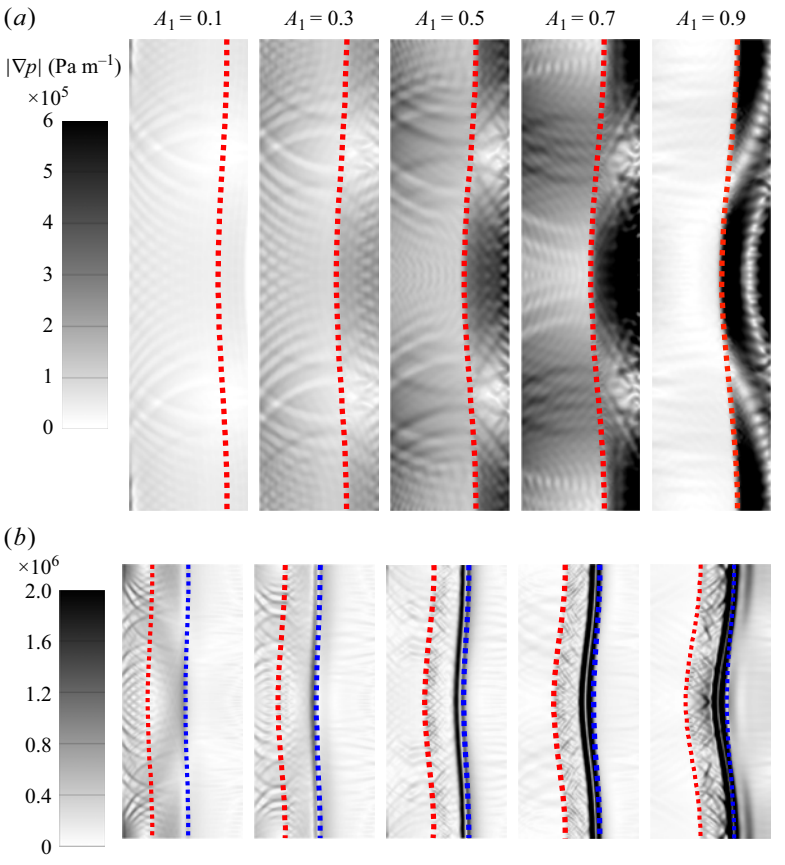


Figure 6. Pressure gradient of the flow near the UI at the moment when TS just forms in the layer (*a*), and the flow near the layer after TS passes through the DI (*b*). The red and blue dotted lines represent the position of UI and DI, respectively.

eliminates the phase reversal of the DI perturbation, which explains the initially growing DI fundamental mode in $A_1 = 0.9$. As a result, effects of A_1 on the DI perturbation growth may be distinguished into three different phases, but their boundaries are not clear now.

Moreover, as revealed in previous works (Wouchuk & López Cavada 2004; Calvo-Rivera, Velikovich & Huete 2023; Napieralski *et al.* 2024), after the IS passes the UI, the resulting perturbed TS propagates through the layer and radiates perturbed acoustic waves back towards the UI to establish mechanical equilibrium. These acoustic waves reverberate within the layer and influence perturbation growth at both the UI and DI, as indicated by the oscillatory behaviour observed in the growth curves in figure 4. As a result, studying the Atwood-number dependence of these acoustic waves is essential for a thorough understanding of RMI evolution in a layered configuration. To isolate the effect of the Atwood number on perturbed acoustic waves without interference from zero-order reflected waves, we analyse behaviour of acoustic waves under total-transmission condition. The propagation of acoustic waves within the layer is visualized by extracting the pressure gradient $|\nabla p|$ in the flow near the interfaces. For the numerical cases with varying A_1, we focus on two key instants: the moment when the TS is initially generated inside the layer, and the time when this shock just departs from the DI, as illustrated in figures 6(*a*) and 6(*b*), respectively.

https://doi.org/10.1017/jfm.2025.11064 Published online by Cambridge University Press

As shown in figure 6(*a*), an increase in A_1 leads to a stronger pressure disturbance propagating from the shocked UI towards the DI. This indicates that a higher A_1 amplifies the initial acoustic waves, which in turn influence the subsequent RMI evolution at the DI. After the shock fully traverses the layer (figure 6*b*), the reverberating acoustic waves remain weak and barely observable at low A_1 values. However, as A_1 exceeds 0.5, these waves coalesce into a conspicuous, single-mode wave system inside the layer. This coherent wave structure, which grows increasingly prominent with higher A_1, exhibits stronger pressure gradients and occupies a broader region, exerting a significant influence on the evolution of both the DI and UI.

In the present study, the IS is relatively weak and all fluid media are gaseous. Under these conditions, the incompressible flow models employed in our derivations provide reasonably accurate predictions for both the linear and nonlinear growth of perturbations at the shocked layer. Given the good agreement observed between these model predictions and the numerical results, a quantitative modelling of the acoustic wave propagation and its influence on the RMI is not pursued in this work. Nevertheless, it is recognized that the incompressible theory becomes increasingly inaccurate when compressibility effects are significant, such as in scenarios involving strong IS. In future studies, we intend to adopt a compressible theoretical framework to quantitatively analyse the role of acoustic waves in modulating the amplitude evolution. A model capable of accurately quantifying the acoustic wave effects in multi-interface RMI under strong shock conditions is expected to develop.

In summary, at lower A_1, interface coupling exerts a significantly more pronounced influence on the UI than on the DI, and causes phase reversal to occur in light–heavy UI where it normally should not manifest. Conversely, at higher A_1, interface coupling has a much stronger effect on the DI than on the UI, and prevents phase reversal from occurring in heavy–light DI where it normally would be expected. Furthermore, there is a critical A_1 yielding $\psi = 0$ for either the UI or DI, revealing that when reverberating waves are eliminated, the freeze-out can be achieved at either the UI or DI under a specific Atwood-number condition of the layer.

3.2. *Modulation of RMI under total-transmission condition*

Systematic variation of the initial layer width modulates RMI growth in shocked layer with a perturbed interface and planar interface through reverberating waves (Zhou *et al.* 2025*a*; Chen *et al.* 2025*a*). For the layer with two perturbed interfaces, conventional RMI control relies on specific UI/DI amplitude combinations (Mikaelian 1996; Sterbentz *et al.* 2022; Liang & Luo 2023; Cong *et al.* 2024). However, precise fabrication of such amplitude/wavelength configurations proves impractical for ICF targets (Mikaelian 1996). By selecting ablative materials, the Atwood numbers of interfaces in ICF targets can be effectively controlled. This alteration of Atwood numbers may enable direct tuning of RMI growth during ignition. In order to figure out the approach of modulating multi-interface RMI via adjusting Atwood numbers and the parameters defining the modulation of perturbation growth at a shocked layer, we derive the following two dimensionless expressions for the linear growth rates of the UI amplitude (a_1) and DI amplitude (a_2) by further developing (3.6)–(3.7):

$$\frac{\dot{a}_1^{lin}}{k\Delta u_1 a_{1+}} = \frac{A_1(1+A_2) + A_1(1-A_2)\coth(k*L) + \alpha A_2(1+A_1)\mathrm{csch}(kL)}{1 - A_1A_2 + (1+A_1A_2)\coth(kL)}, \tag{3.16}$$

$$\frac{\dot{a}_2^{lin}}{k\Delta u_1 a_{1+}} = \frac{\alpha A_2(1-A_1) + \alpha A_2(1+A_1)\coth(k*L) + A_1(1-A_2)\mathrm{csch}(kL)}{1 - A_1A_2 + (1+A_1A_2)\coth(kL)}. \tag{3.17}$$

https://doi.org/10.1017/jfm.2025.11064 Published online by Cambridge University Press

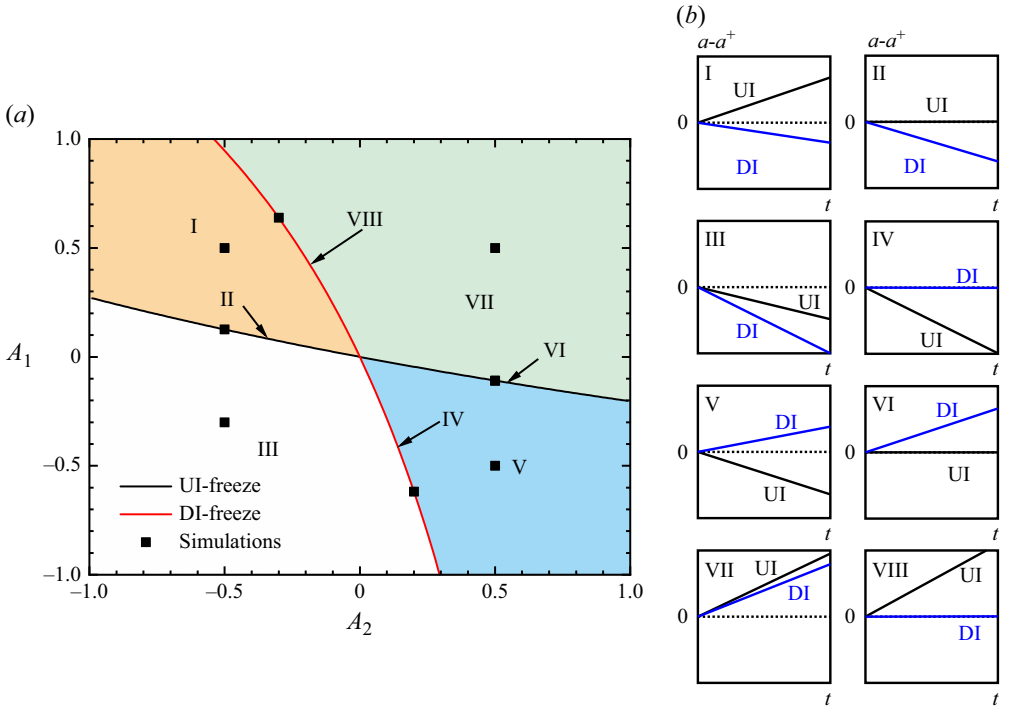


Figure 7. (*a*) Distribution of the manipulation possibilities of the perturbation growth at the UI and DI in (A_2, A_1) domain; (*b*) schematics of the temporal evolution of UI and DI amplitudes in the eight possibilities.

Here, $\alpha = (\rho_{30} - \rho_{20})\Delta u_2 a_{2-} + (\rho_{3+} - \rho_{2+})\Delta u_2 a_{2+}/2(\rho_{3+} - \rho_{2+})\Delta u_1 a_{1+}$, which mainly reflects the ratio of amplitudes of two interfaces. Based on the derived model, the modulation of RMI at a fluid layer can be characterized by four dimensionless parameters: A_1, A_2, α and kL. Notably, this model is applicable to a shocked layer under total-transmission condition. By fixing $\alpha = 0.78$ and $kL = 1.21$, consistent with the conditions in case TT/0.50/−0.50, we use the model to establish the relationships between A_1 and A_2 required to achieve perturbation growth stagnation at either the UI or DI. This relationship is illustrated in the figure 7(*a*). These two curves in the figure are defined as the freezing lines, which means the perturbation growth stagnation can be realized at either the UI or DI when the (A_2, A_1) coordinate locates at these two characteristic curves.

Based on figure 7(*a*) and extensive additional calculations under various combinations of α and kL, it is observed that the curves corresponding to RMI freeze-out at the UI and DI always intersect at ($A_2 = 0$, $A_1 = 0$). This indicates that simultaneously freezing perturbation growth at both interfaces by adjusting only the Atwood numbers, at a layer under total-transmission condition, is theoretically unattainable. The two curves in figure 7(*a*) delineate eight distinct regimes of RMI modulation possibilities, categorized by the direction of amplitude growth at the UI and DI. The temporal amplitude evolution of both UI and DI for the eight possibilities are sketched in figure 7(*b*). By systematically selecting A_2 and A_1 values in the initial configurations, we conduct eight numerical simulations to realize each of these modulation scenarios. The initial settings of the eight cases corresponding to different possibilities are detailed in table 4 and the corresponding amplitude evolutions of both interfaces, extracted from these simulations, are presented in figure 8. The wavelength of perturbation in all the simulations is 40 mm. The different

https://doi.org/10.1017/jfm.2025.11064 Published online by Cambridge University Press

Case	ka_{1-}	ka_{2-}	ρ_{10}	ρ_{20}	ρ_{30}	γ_1	γ_2	γ_3	M_{IS}	L_0	Possibility
MT/0.50/−0.50	0.100	0.100	1.964	5.976	2.864	1.094	1.094	2.641	1.300	10	I
MT/0.13/−0.50	0.100	0.091	4.638	5.976	2.864	1.094	1.094	2.641	1.367	10	II
MT/-0.30/−0.50	0.100	0.128	11.130	5.976	2.864	1.094	1.094	2.641	1.479	10	III
MT/−0.62/0.20	0.110	0.109	9.730	2.279	3.069	1.667	1.667	1.185	1.320	8.7	IV
MT/−0.50/0.50	0.100	0.120	6.657	2.210	4.951	2.600	2.600	1.027	1.281	8.4	V
MT/−0.11/0.50	0.100	0.109	2.751	2.210	4.951	2.600	2.600	1.027	1.213	8.5	VI
MT/0.50/0.50	0.100	0.087	0.735	2.210	4.951	2.600	2.600	1.027	1.155	8.4	VII
MT/0.64/−0.30	0.100	0.109	1.314	5.976	4.092	1.094	1.094	1.750	1.277	10	VIII
MT-AP/0.14/0.50	0.130	−0.135	1.113	1.473	3.300	2.600	2.600	1.027	1.186	8.4	Freezing UI
MT-AP/−0.57/−0.30	0.110	−0.081	8.502	2.302	1.432	1.094	1.094	1.873	1.304	9.0	Freezing DI

Table 4. Initial conditions of numerical cases for realizing different possibilities of RMI growth at an in-phase layer and freezing perturbation growth at interfaces of an antiphase layer under the total-transmission condition. Here ka_{1-} and ka_{1-} are the initial scaled amplitudes of UI and DI, respectively. The symbols have the same meaning as those in table 3. The units of density and width are kg m^{-3} and mm, respectively.

initial scaled interface amplitudes (ka_1 and ka_2) and layer widths (L_0) are set to fix the dimensionless parameter α and layer width when TS impacting DI ($L = L_0(1 - \Delta u_1/v_1^t)$). Results confirm that all eight modulation possibilities are successfully reproduced in the simulations and align closely with the predictions of the models (3.16)–(3.17). It should be noted that the defined modulation possibilities encompass not only the case of a shocked heavy layer ($A_2 < 0$ and $A_1 > 0$) but also layers with all other possible combinations of A_2 and A_1.

To further validate the universality of our models, we also simulate cases involving layers with antiphase initial perturbations ($\alpha < 0$), as detailed in table 4. With α and kL set to -0.78 and 1.21 respectively, two specific combinations of A_2 and A_1, predicted by the dimensionless models (3.16)–(3.17) to induce RMI stagnation at either the UI or DI, are numerically tested. The computed perturbation amplitude evolutions for both interfaces are plotted in the figure 9. As evidenced by the results, amplitude growth stagnation is successfully achieved at the targeted interface in each case, confirming the model's capability to accurately predict stagnation conditions in initially antiphase layers.

3.3. *Atwood-number dependence under non-total-transmission condition*

In practical scenarios, the total transmission condition is unattainable, resulting in persistent wave reverberations within the shocked layer. For shock-accelerated heavy layers, as shown in figure 1(*d*), these reverberation waves comprise RW generated when TS impacts DI and CW reflected from RW–UI interaction. Similar to that in § 3.1, the initial perturbations for both interfaces are with fixed $ka = 0.1$ and $\lambda = 40$ mm, and the initial layer width $L_0 = 10$ mm. To investigate the Atwood-number dependence of multi-interface RMI in a heavy layer with reverberating waves, we conduct simulations in which both A_1 and A_2 were systematically varied. In all cases for this part, the adiabatic index is set to 1.67. For investigating A_1 dependence, the initial configurations are set similarly to those in the preceding part: the upstream fluid density (ρ_{10}) is altered to vary A_1, while the densities of the other fluids are maintained. Concurrently, the IS Mach number is adjusted in each case to ensure a constant TS Mach number within the layer, thereby isolating the A_1 effect from changes in shock compressing DI. For investigating A_2 dependence, the densities of the fluids upstream and within the layer are held constant, fixing A_1. The downstream

https://doi.org/10.1017/jfm.2025.11064 Published online by Cambridge University Press

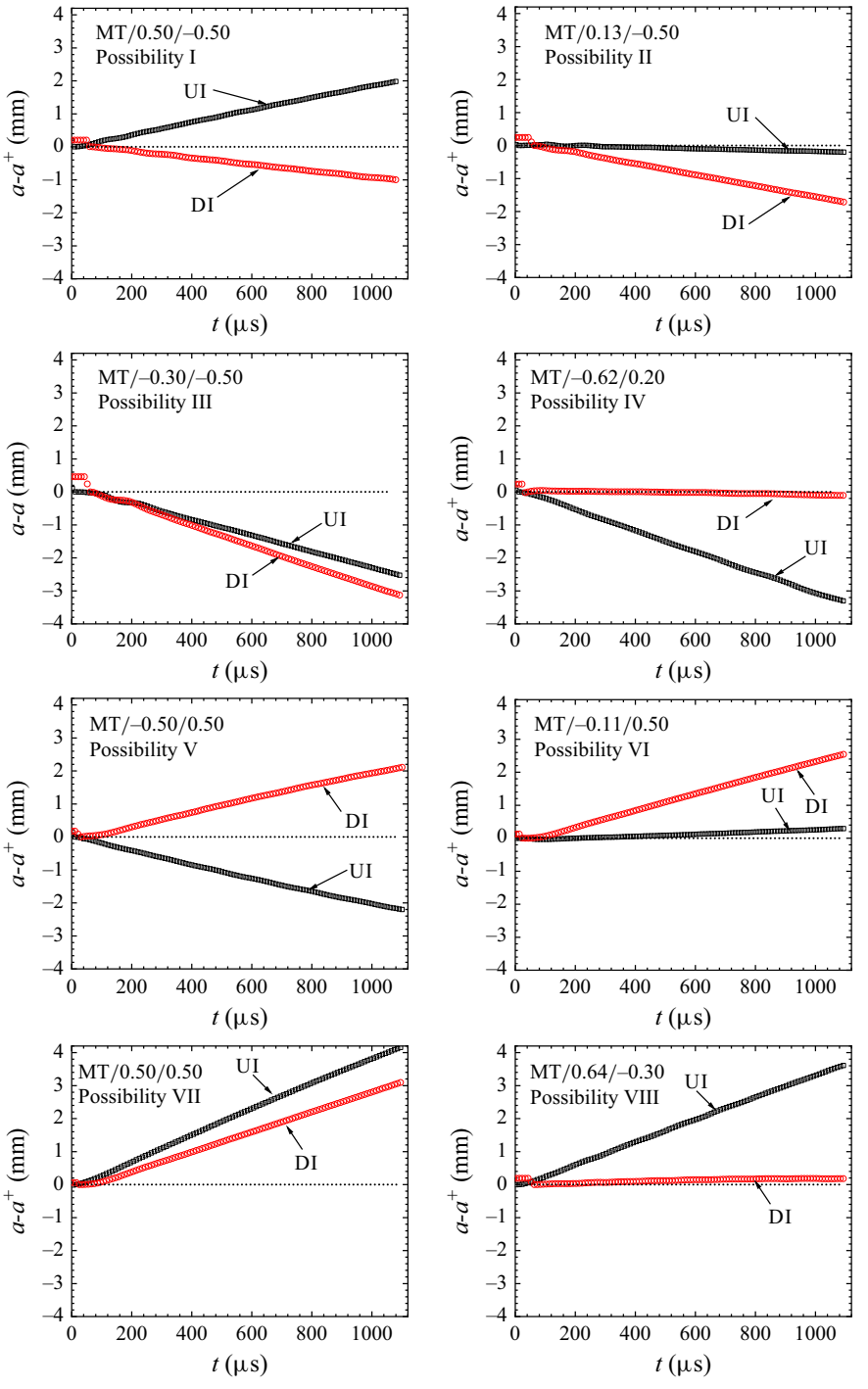


Figure 8. Temporal amplitude evolution of both the UI and DI in the simulations designed for the eight different modulation possibilities of RMI at an in-phase layer.

https://doi.org/10.1017/jfm.2025.11064 Published online by Cambridge University Press

Case	A_1	A_2	φ_1	φ_2	φ_3	ρ_{10}	ρ_{20}	ρ_{30}	M_{IS}	M_{TS}
0.10/−0.50	0.10	−0.50	0.811	1	0.311	4.388	5.372	1.784	1.246	1.259
0.50/−0.10	0.50	−0.10	0.311	1	0.811	1.784	5.372	4.388	1.200	1.259
0.50/−0.50	0.50	−0.50	0.311	1	0.311	1.784	5.372	1.784	1.200	1.259
0.50/−0.90	0.50	−0.90	0.311	1	0.022	1.784	5.372	0.278	1.200	1.259
0.90/−0.50	0.90	−0.50	0.022	1	0.311	0.278	5.372	1.784	1.153	1.259

Table 5. Initial parameters of the numerical cases designed to investigate the Atwood-number dependence of RMI at a helium/xenon/helium layer with reverberating waves. Here φ_1, φ_2 and φ_3 denote the volume fractions of xenon in gases 1, 2 and 3, respectively; 1-φ_1, 1-φ_2 and 1-φ_3 denote the volume fractions of helium in gases 1, 2 and 3, respectively.

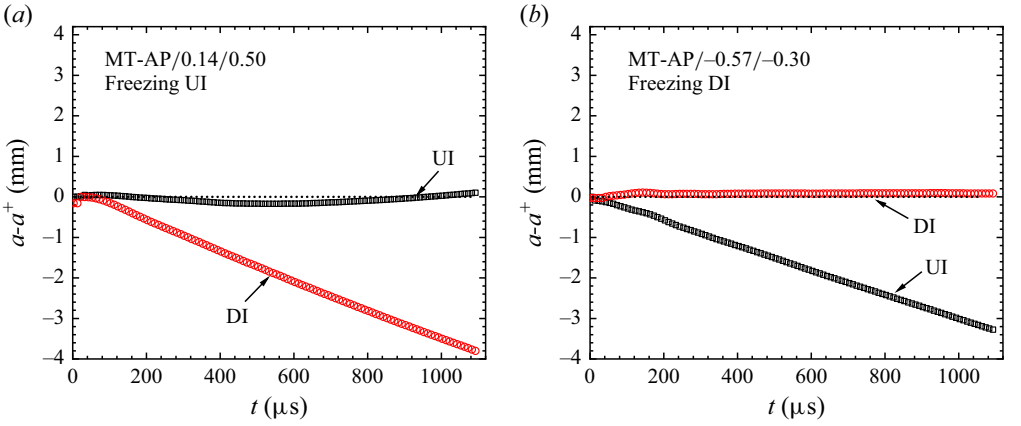


Figure 9. Amplitude evolution of the interfaces of an initial antiphase layer in the simulations designed for realizing RMI stagnation at the UI (*a*) and DI (*b*).

fluid density is then varied to achieve different A_2 values. In these simulations, the IS Mach number is fixed at 1.20. This configuration ensures that the initial jump velocities of both interfaces remain unchanged across cases, allowing the observed differences to be attributed solely to A_2. The complete set of initial parameters for these cases is provided in table 5. The cases are labelled as A_1/A_2 to denote Atwood-number combinations.

Figure 10 presents schlieren images of layer evolution for all five reverberating-wave cases. Wave structures resemble those in figure 3, with notable RW emerging from TS–DI interactions. Following shock traversal through the layer, both the UI and DI remain single-mode. At the late stage, the perturbation growth exhibits pronounced sensitivity to A_1 and A_2. When A_2 is fixed, the DI mixing width inversely correlates with A_1, while DI transitions to multimode morphology at higher A_1. The UI exhibits accelerated growth and enhanced nonlinearity (bubbles, spikes, roll-ups) with increasing A_1. When A_1 is fixed, the UI mixing widths remain comparable, but asymmetry intensifies with A_2 increasing. Specifically, the roll-up structures form at the UI spike when $A_2 = -0.9$. The DI amplitude grows with higher A_2, and the phase inversion is suppressed when $A_2 = -0.1$. Similar to the UI, the DI asymmetry accelerates at higher A_2.

https://doi.org/10.1017/jfm.2025.11064 Published online by Cambridge University Press

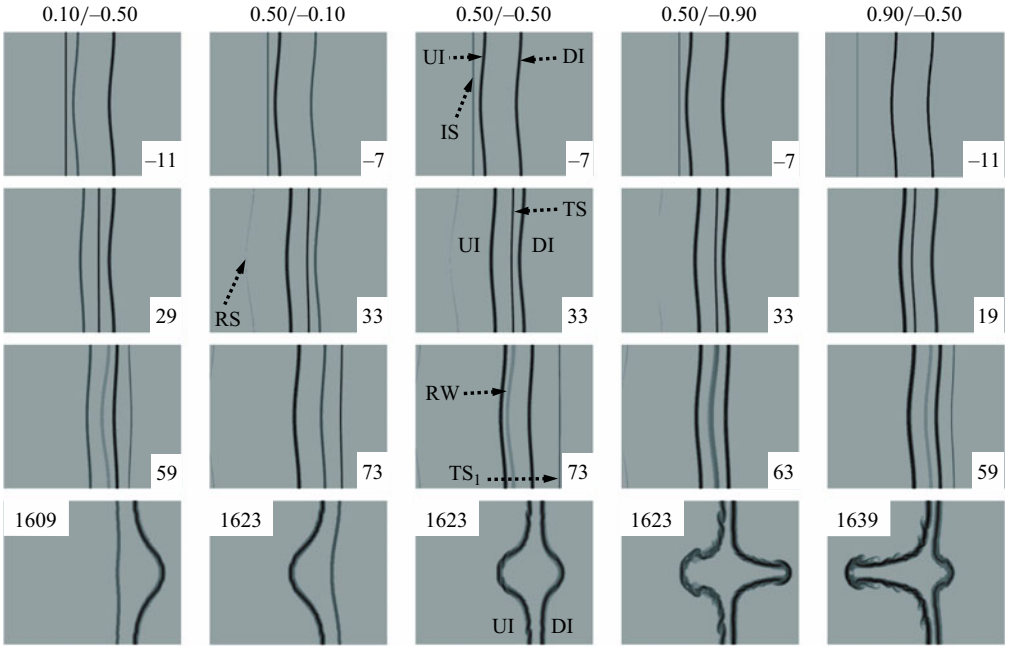


Figure 10. Schlieren images of the shock-induced helium/xenon/helium layer evolution under different Atwood-number conditions.

Given the absence of theoretical frameworks for harmonic evolution in shocked layers and the persistent dominance of basic modes, as shown in figure 10, we analyse basic-mode growth at the UI and DI via FFT analysis, as presented in figure 11. For the UI of a heavy layer, both IS and RW induce acceleration directed from light to heavy fluids. Therefore, assuming the initial UI phase is defined as positive, the effects of both IS and RW on the UI amplitude are positive. The accelerations of the DI induced by TS and CW within the layer are both from heavy to light fluids, indicating that the effects of TS and CW on the DI amplitude are negative. Figure 11(*b*) shows that for the DI, the intensified interface coupling at elevated A_1 causes the basic mode amplitude of the DI to grow into a negative phase at an attenuated rate. This behaviour aligns with the phenomenology observed in figure 4. In case 0.10/−0.5, the fundamental mode amplitude at the UI evolves to the negative phase. This occurs because the interface-coupling effect overcomes the positive effects of IS and RW. However, for cases 0.50/−0.5 and 0.90/−0.5, the perturbation amplitude on the UI increases consistently, governed by the dominant effects of IS and RW. Figure 11(*d*) reveals that in case 0.50/−0.10, the fundamental mode of the DI evolves to a positive phase. This results from interface coupling governing the fundamental mode of the DI. When A_1 and M_{IS} are fixed as 0.5 and 1.2, respectively, the effect of IS on the UI perturbation remains constant. Therefore, the non-monotonic relationship between A_2 and the UI amplitude growth rate observed in figure 11 results from mutual cancellation between the RW effect and the interface coupling contribution.

To quantify the coupled effects of wave reverberating and interface coupling on multi-interface RMI across varying Atwood-numbers, we adopt a linear model. In our prior work (Chen *et al.* 2025*b*), the models incorporating different interface accelerations arising from

https://doi.org/10.1017/jfm.2025.11064 Published online by Cambridge University Press

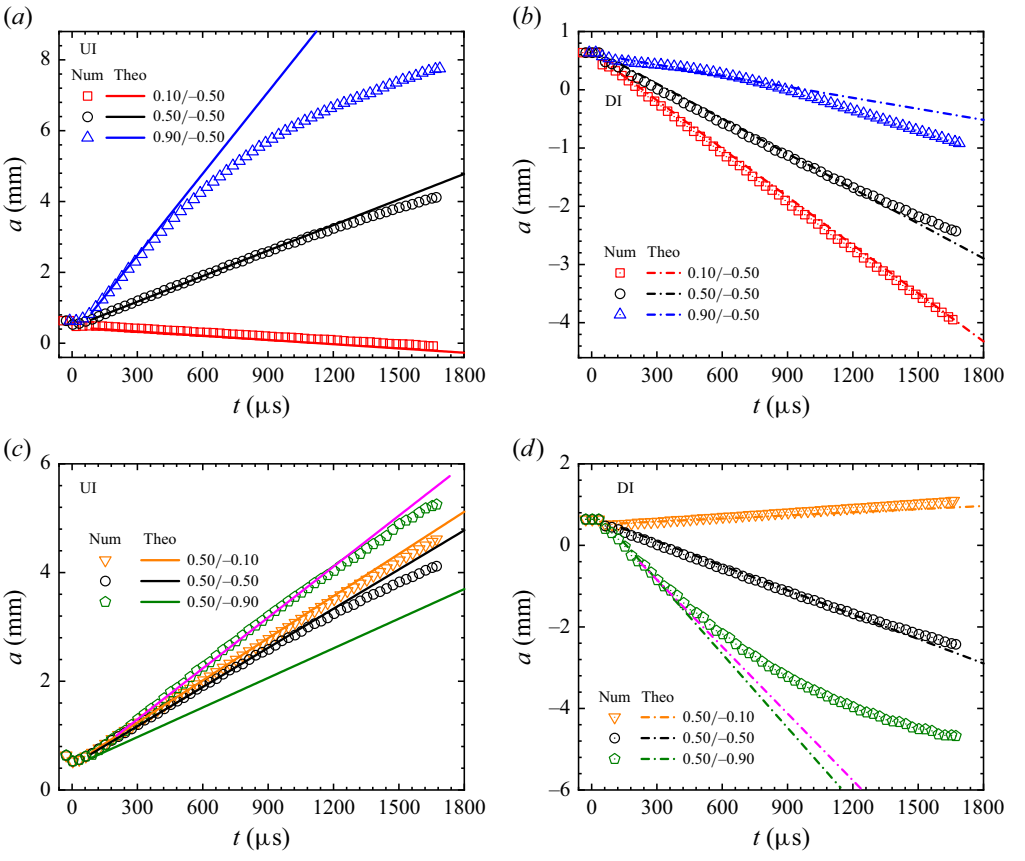


Figure 11. Comparison of the fundamental mode amplitude between numerical results (symbols) and predictions (lines matching the colour of the symbols) from models incorporating two reverberating waves for UI and DI in cases with fixed A_2 (*a*,*b*) and cases with fixed A_1 (*c*,*d*). The pink lines in (*c*) and (*d*) denote the theoretical predictions from models incorporating four reverberating waves.

reverberating waves inside a shocked three-fluids layer, are expressed as

$$\begin{cases} \dfrac{d^2a_1}{dt^2}[\rho_1+\rho_2\tanh(kL/2)]+\dfrac{d^2a_2}{dt^2}[\rho_3+\rho_2\tanh(kL/2)] \\ \quad =k[(\rho_2-\rho_1)a_1g_1+(\rho_3-\rho_2)a_2g_2], \\ \dfrac{d^2a_1}{dt^2}[\rho_1+\rho_2\coth(kL/2)]-\dfrac{d^2a_2}{dt^2}[\rho_3+\rho_2\coth(kL/2)] \\ \quad =k[(\rho_2-\rho_1)a_1g_1-(\rho_3-\rho_2)a_2g_2]. \end{cases} \tag{3.18}$$

When both the UI jump velocities induced by IS (Δu_1) and RW (Δu_{RI}), and DI jump velocities induced by TS (Δu_2) and CW (Δu_{C1}) are considered, g_1 and g_2 can be expressed as

$$\begin{cases} g_1=\Delta u_1\delta t+\Delta u_{RI}\delta(t-t_2), \\ g_2=\Delta u_2\delta(t-t_1)+\Delta u_{C1}\delta(t-t_3), \end{cases} \tag{3.19}$$

https://doi.org/10.1017/jfm.2025.11064 Published online by Cambridge University Press

where t_2 and t_3 are the instants when RW arrive at the UI and CW interact with the DI, respectively, and are expressed as

$$\begin{cases} t_2 = t_1 + L_0(1 - \Delta u_1/v_1^t)/c_1, \\ t_3 = t_2 + L_0(1 - \Delta u_1/v_1^t)[1 + (\Delta u_2 - \Delta u_1)/c_1]/c_2. \end{cases} \tag{3.20}$$

By substituting (3.19) into (3.18) and applying the impulsive model to IS-driven UI acceleration and the VMG model to TS-driven DI acceleration, we integrate (3.18) to establish linear growth models for the fundamental mode amplitudes of the UI and DI:

$$\begin{aligned} &\dot{a}_1^{lin}[\rho_{1R} + \rho_{2R}\tanh(kL/2)] + \dot{a}_2^{lin}[\rho_{3C} + \rho_{2C}\tanh(kL/2)] \\ &\quad = k\Delta u_1(\rho_{2+} - \rho_{1+})a_{1+} + k\Delta u_{RI}(\rho_{2R} - \rho_{1R})a_{1R} \\ &\qquad + k\Delta u_2[(\rho_{30} - \rho_{20})a_{2-} + (\rho_{3+} - \rho_{2+})a_{2+}]/2 + k\Delta u_{C1}(\rho_{3C} - \rho_{2C})a_{2C}, \end{aligned} \tag{3.21}$$

$$\begin{aligned} &\dot{a}_1^{lin}[\rho_{1R} + \rho_{2R}\coth(kL/2)] - \dot{a}_2^{lin}[\rho_{3C} + \rho_{2C}\coth(kL/2)] \\ &\quad = k\Delta u_1(\rho_{2+} - \rho_{1+})a_{1+} + k\Delta u_{RI}(\rho_{2R} - \rho_{1R})a_{1R} \\ &\qquad - k\Delta u_2[(\rho_{30} - \rho_{20})a_{2-} + (\rho_{3+} - \rho_{2+})a_{2+}]/2 - k\Delta u_{C1}(\rho_{3C} - \rho_{2C})a_{2C}. \end{aligned} \tag{3.22}$$

Here ρ_{1R} and ρ_{2R} denote the densities of gases 1 and 2 after RW hit the UI, respectively; ρ_{2C} and ρ_{3C} denote the densities of gases 2 and 3 after CW impact the DI, respectively; a_{1+} (the UI amplitude post-IS acceleration) and a_{2+} (the DI amplitude post-TS acceleration) can be calculated via equations in § 3.1; a_{1R} denotes the UI amplitude immediately after RW impact. Accounting for the startup process, the UI amplitude prior to RW impact is given by

$$\begin{cases} a_{1R-} = a_{1+} + \int_{t_1^c}^{t_2} \frac{2\dot{a}_1^{lin}}{(1+A_1)\coth(kL_{T1}) + (1-A_1)\coth(kL_{F1})}\mathrm{d}t \\ (t_2 < t_1^c + t_1^{st}), \\ a_{1R-} = a_{1+} + \int_{t_1^c}^{t_1^c + t_1^{st}} \frac{2\dot{a}_1^{lin}}{(1+A_1)\coth(kL_{T1}) + (1-A_1)\coth(kL_{F1})}\mathrm{d}t + (t_2 - t_1^c - t_1^{st})\dot{a}_1^{lin} \\ (t_2 \geqslant t_1^c + t_1^{st}). \end{cases} \tag{3.23}$$

Here, t_1^{st}, L_{F1} and L_{T1} are defined in (3.3)–(3.5). To quantify RW–UI interaction, we consider RW amplitude dynamics. When RW originate from TS impacting the DI, the initial RW amplitudes are

$$\begin{cases} a_{R0} = (a_{Rf0} + a_{Rt0})/2, \\ a_{Rf0} = a_{2-} - (a_{2-} - a_{s1})(c_1 - \Delta u_1)/v_1^t, \\ a_{Rt0} = a_{2-} - (a_{2-} - a_{s1})(c_2 - \Delta u_2)/v_1^t, \end{cases} \tag{3.24}$$

where c_1 and c_2 denote sound speeds in gas 2 (RW front to the UI and RW tail to the DI regions, respectively), a_{s1} is given by (3.9). The RW tail amplitude evolves during moving within the layer as (Velikovich & Phillips 1996)

$$\dot{a}_{Rt} = -ka_{Rf0}c_1\sqrt{(\gamma_2 + 1)(1 - c_2/c_1)/(\gamma_2 - 1)}. \tag{3.25}$$

Since the RW front amplitude remains constant, the RW amplitude at the moment of impacting UI is

$$a_{R1} = a_{R0} + \dot{a}_{Rt}(t_2 - t_1)/2. \tag{3.26}$$

https://doi.org/10.1017/jfm.2025.11064 Published online by Cambridge University Press

Based on (3.23)–(3.26), the UI amplitude immediately after RW impact can be expressed as

$$a_{1R} = a_{1R-} + (a_{1R-} - a_{R1})\frac{\Delta u_{RI}}{c_1 + c_2 + \Delta u_1 - \Delta u_2}. \tag{3.27}$$

In (3.21)–(3.22), a_{2C} (the DI amplitude post-CW impact) incorporates the DI startup process,

$$\begin{cases} a_{2C-} = a_{1+} + \int_{t_1+t_2^c}^{t_3} \frac{2\dot{a}_2^{lin}}{(1+A_2)\coth(kL_{T2})+(1-A_2)\coth(kL_{F2})}\mathrm{d}t \\ (t_3 < t_1 + t_2^c + t_2^{st}), \\ a_{2C-} = a_{1+} + \int_{t_1+t_2^c}^{t_1+t_2^c+t_2^{st}} \frac{2\dot{a}_2^{lin}}{(1+A_2)\coth(kL_{T2})+(1-A_2)\coth(kL_{F2})}\mathrm{d}t + (t_3 - t_1 - t_2^c - t_2^{st})\dot{a}_2^{lin} \\ (t_3 \geqslant t_1 + t_2^c + t_2^{st}), \end{cases} \tag{3.28}$$

where t_2^{st}, L_{F2} and L_{T2} are defined in (3.11)–(3.13). The CW amplitude after reflection by RW interacting with the UI is

$$\begin{cases} a_{C0} = (a_{Cf0} + a_{Ct0})/2, \\ a_{Cf0} = a_{1R-} - (a_{1R-} - a_{Rf0})(c_2 + \Delta u_2 - \Delta u_1)/c_1, \\ a_{Ct0} = a_{1R-} - [a_{1R-} - a_{Rt0} - \dot{a}_{Rt}(t_2 - t_1)](c_3 + \Delta u_{RI})/c_2. \end{cases} \tag{3.29}$$

Here, a_{1R-}, a_{Rt0}, a_{Rf0} and $\dot{a}_{Rt}$ are calculated from (3.23)–(3.25); c_3 is the sound speed of gas 2 between CW tail and the UI. Given the CW's weakness and brief transit, its amplitude variation is neglected. The DI amplitude after CW passage is

$$a_{2C} = a_{2C-} - (a_{2C-} - a_{C0})\frac{2\Delta u_{C1}}{c_3 + c_2 + \Delta u_{RI} + \Delta u_1 - \Delta u_2}. \tag{3.30}$$

In conclusion, (3.21)–(3.30) determine the linear growth rates for the UI and DI amplitudes.

As shown in figure 11, the theoretically predicted curves exhibit strong agreement with numerical results during the linear stage, excepting the maximum A_2 configuration. For case 0.50/−0.90 (figure 11*c*,*d*), the green theoretical lines derived from (3.21)–(3.22) display significant divergence from simulated UI amplitudes. Because a high amplitude of A_2 intensifies reverberating waves generated by wave–DI interactions, the deviation in (3.21)–(3.22) stems from neglecting additional reflected waves within the layer during derivation.

Figures 12(*a*) and 12(*b*) show temporally averaged x-direction velocities of interface nodes from cases 0.90/−0.50 and 0.50/−0.90, respectively. Dotted lines represent one-dimensional gas theory predictions considering only RW and CW. Note that based on the constraints in numerically extracting flow parameters with limited temporal resolution, the simulated results cannot precisely capture the ideal instantaneous velocity jumps at the interfaces. As a result, deviations from the one-dimensional ideal-gas theory may occur during the very brief period of wave–interface interactions. The final interface velocity, which stabilizes after approximately 400 μs, reflects the cumulative effect of velocity jumps induced by all relevant wave–interface interactions. For high A_1 configurations (figure 12*a*), the second gas theory (incorporating first and second reflected waves) accurately predicts the UI and DI velocities. However, for enhanced A_2 cases (figure 12*b*), this theory shows discrepancies, particularly for the UI. Thus, accurate acceleration prediction for high-A_2 layers requires additional reverberating waves. Solid lines in figure 12(*b*) show fourth gas theory predictions incorporating four waves: RW, CW, RW_2

https://doi.org/10.1017/jfm.2025.11064 Published online by Cambridge University Press

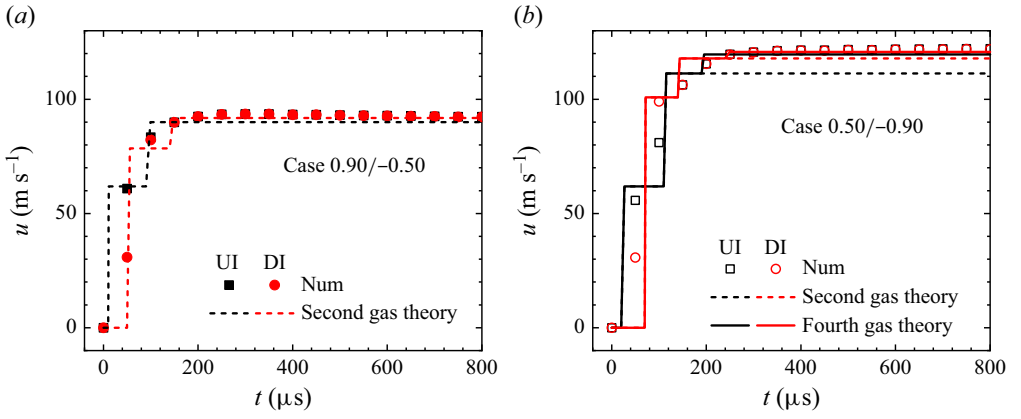


Figure 12. Comparison of the interface velocities in the x-direction of the shocked heavy layer between the numerical results (symbols) and predictions (lines) from one-dimensional gas theory for case 0.90/−0.50 (*a*) and case 0.50/−0.90 (*b*).

(rarefaction waves from CW-DI interaction) and CW_2 (from RW_2-UI interaction). This fourth gas theory accurately predicts the UI and DI accelerations for case 0.50/−0.90. We therefore reformulate (3.21)–(3.22) as

$$\begin{aligned}&\dot{a}_1^{lin}[\rho_{1R}+\rho_{2R}\tanh(kL/2)]+\dot{a}_2^{lin}[\rho_{3C}+\rho_{2C}\tanh(kL/2)]\\&=k\Delta u_1(\rho_{2+}-\rho_{1+})a_{1+}+k\Delta u_{RI}(\rho_{2R}-\rho_{1R})a_{1R}+k\Delta u_{R2}(\rho_{2R2}-\rho_{1R2})a_{1R2}\\&\quad+k\Delta u_2[(\rho_{30}-\rho_{20})a_{2-}+(\rho_{3+}-\rho_{2+})a_{2+}]/2\\&\quad+k\Delta u_{C1}(\rho_{3C}-\rho_{2C})a_{2C}+k\Delta u_{C2}(\rho_{3C2}-\rho_{2C2})a_{2C2},\end{aligned}\tag{3.31}$$

$$\begin{aligned}&\dot{a}_1^{lin}[\rho_{1R}+\rho_{2R}\coth(kL/2)]-\dot{a}_2^{lin}[\rho_{3C}+\rho_{2C}\coth(kL/2)]\\&=k\Delta u_1(\rho_{2+}-\rho_{1+})a_{1+}+k\Delta u_{RI}(\rho_{2R}-\rho_{1R})a_{1R}+k\Delta u_{R2}(\rho_{2R2}-\rho_{1R2})a_{1R2}\\&\quad-k\Delta u_2[(\rho_{30}-\rho_{20})a_{2-}+(\rho_{3+}-\rho_{2+})a_{2+}]/2\\&\quad-k\Delta u_{C1}(\rho_{3C}-\rho_{2C})a_{2C}-k\Delta u_{C2}(\rho_{3C2}-\rho_{2C2})a_{2C2},\end{aligned}\tag{3.32}$$

where Δu_{R2} (Δu_{C2}), ρ_{1R2} and ρ_{2R2} (ρ_{2C2} and ρ_{3C2}) denote the jump velocity of the UI (DI) induced by RW_2 (CW_2), the densities of gas 1 and gas 2 (gas 2 and gas 3) after RW_2 impact the UI (CW_2 impact the DI), respectively. Here a_{1R2} (the post-RW_2 UI amplitude) and a_{2C2} (the post-CW_2 DI amplitude) are

$$\begin{cases}a_{1R2}=a_{1R}+\dot{a}_1^{lin}(t_4-t_2),\\a_{2C2}=a_{2C}+\dot{a}_2^{lin}(t_5-t_3).\end{cases}\tag{3.33}$$

Here, t_4 and t_5 are the specific moments when RW_2 impact the UI and CW_2 accelerate the DI, respectively, and are calculated as

$$\begin{cases}t_4= & t_3+L_0(1-\Delta u_1/v_1^t)[1+(\Delta u_2-\Delta u_1)/c_1]\\ & \times[1-(\Delta u_1+\Delta u_{RI}-\Delta u_2)/c_2]/c_3,\\t_5= & t_4+L_0(1-\Delta u_1/v_1^t)[1+(\Delta u_2-\Delta u_1)/c_1]\\ & \times[1-(\Delta u_1+\Delta u_{RI}-\Delta u_2)/c_2][1+(\Delta u_2+\Delta u_{R2}-\Delta u_1-\Delta u_{RI})/c_3]/c_4,\end{cases}\tag{3.34}$$

where c_4 is the sound speed of gas 2 between RW_2 tail and the DI. Pink lines in figure 11(*c*,*d*) show predictions from (3.31)–(3.32) for case 0.50/−0.90. This refined

https://doi.org/10.1017/jfm.2025.11064 Published online by Cambridge University Press

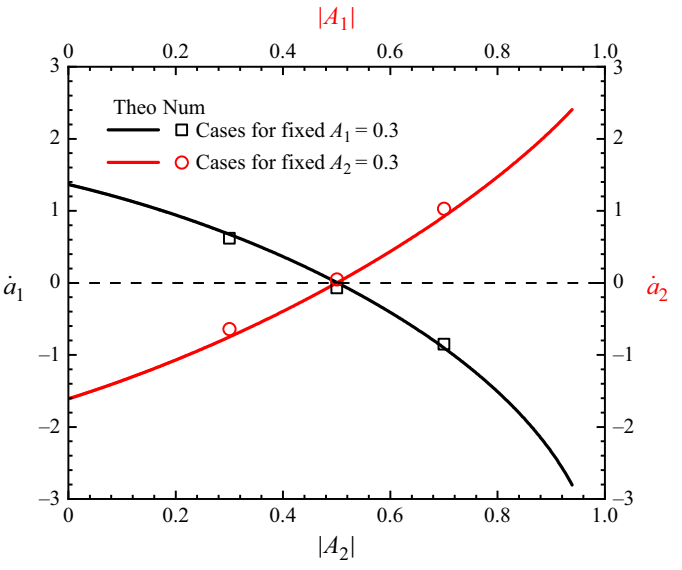


Figure 13. Variations of the amplitude growth rate with Atwood number. The black (red) line represents the amplitude growth rate of the UI (DI) varying with $|A_2|$ ($|A_1|$).

model achieves precise agreement with simulations under high-A_2 conditions through incorporating more reverberating waves.

3.4. *Modulation of RMI under non-total-transmission condition*

Considering the reverberating waves within a shocked layer, we investigate whether RMI growth at a specified interface can be controlled by strategically adjusting the Atwood number of the opposing interface of a shocked layer. To this end, we systematically vary the Atwood numbers A_1 and A_2 to manipulate the perturbation growth at the DI and UI of a shocked layer with reverberating waves, respectively.

In subsequent simulations, λ and L_0 are fixed at 40 and 10 mm, respectively. To control RMI at the DI, we set $ka_{1-} = 0.18$ and $ka_{2-} = 0.1$ with constant $A_2 = 0.3$ and $M_{TS} = 1.259$. For the UI perturbation manipulation, $ka_{1-} = 0.1$ and $ka_{2-} = 0.18$ with fixed $A_1 = 0.3$ and $M_{IS} = 1.20$. Figure 13 shows theoretical predictions from (3.21)–(3.22) for $\dot{a}_2$ versus A_1 (red line) and (3.31)–(3.32) for $\dot{a}_1$ versus A_2 (black line). Null growth rates indicate perturbation freeze-out at the interface (Mikaelian 1985). Six numerical simulations (symbols in figure 13) with initial parameters appearing in table 6 validate this approach, with two distinct configurations achieving freeze-out at either the UI or DI. The cases for modulating the perturbation growth at the DI (UI) via changing the Atwood number of the UI (DI) are named 'M/A_1/A_2' ('M/A_1/A_2').

The schlieren images for all six cases are presented in figure 14. Figure 14(*a–c*) show the DI modulation by varying A_1. When $A_1 = 0.3$, the DI undergoes phase reversal analogous to a shocked single heavy–light interface. When $A_1 = 0.5$, the DI amplitude stagnates (almost from 53-1613 μs). When $A_1 = 0.7$, the UI grows substantially, while the DI evolves in phase-synchronization with the UI. Figure 14(*d–f*) demonstrate the UI modulation via A_2 adjustment. The UI amplitude undergoes amplification when $A_2 = 0.3$ and remains quasistationary when $A_2 = 0.5$. When $A_2 = 0.7$, the basic mode at the UI evolves to the opposite phase with the initial perturbation, synchronizing with the DI evolution.

https://doi.org/10.1017/jfm.2025.11064 Published online by Cambridge University Press

Case	A_1	A_2	φ_1	φ_2	φ_3	ρ_{10}	ρ_{20}	ρ_{30}	M_{IS}	M_{TS}	ka_{1-}	ka_{2-}
M/0.30/−0.30	0.30	−0.30	0.522	1	0.522	2.883	5.372	2.883	1.222	1.259	0.18	0.1
M/0.50/−0.30	0.50	−0.30	0.311	1	0.522	1.784	5.372	2.883	1.200	1.259	0.18	0.1
M/0.70/−0.30	0.70	−0.30	0.150	1	0.522	0.945	5.372	2.883	1.179	1.259	0.18	0.1
M2/0.30/−0.30	0.30	−0.30	0.522	1	0.522	2.883	5.372	2.883	1.200	1.234	0.1	0.18
M2/0.30/−0.50	0.30	−0.50	0.522	1	0.311	2.883	5.372	1.784	1.200	1.234	0.1	0.18
M/0.30/−0.70	0.30	−0.70	0.522	1	0.150	2.883	5.372	0.945	1.200	1.234	0.1	0.18

Table 6. Initial conditions of the simulations designed to realize manipulation of perturbation growth at either the UI or DI. The symbols have the same meaning as those in tables above.

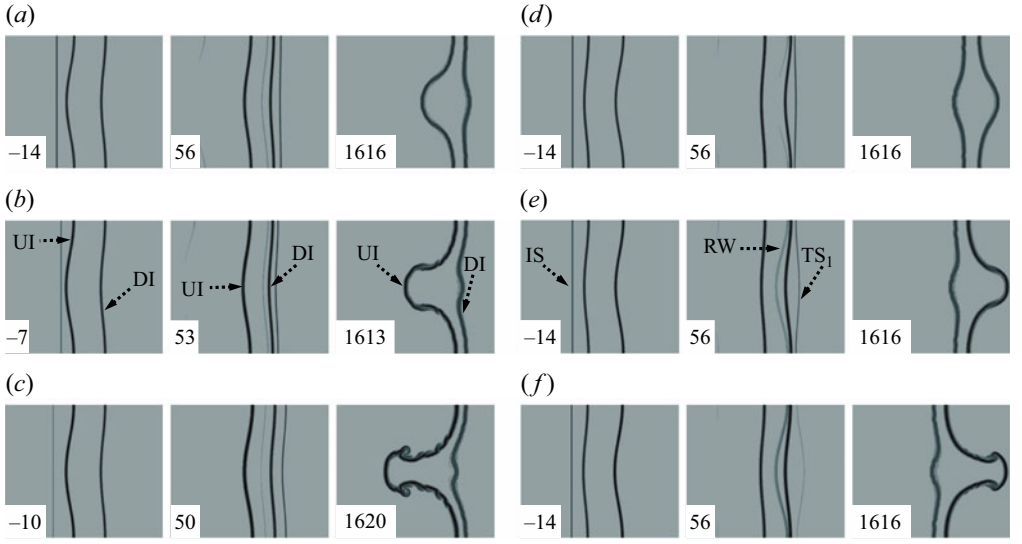


Figure 14. Schlieren images of interface evolution and wave patterns for (*a*) case M/0.30/−0.30, (*b*) case M/0.50/−0.30, (*c*) case M/0.70/−0.30, (*d*) case M2/0.30/−0.30, (*e*) case M2/0.30/−0.50 and (*f*) case M2/0.30/−0.70.

Figure 15 presents temporal evolution of fundamental mode amplitudes at the DI (UI) extracted via FFT from simulations with fixed A_2 (A_1). Quantitative results demonstrate controllable modulation of perturbation growth at either interface through Atwood number variation at the opposite interface. Optimized Atwood-number selection achieves perturbation freeze-out at both the UI and DI. Theoretical predictions from (3.21)–(3.22) (lines in figure 15*a*) and (3.31)–(3.32) (lines in figure 15*b*) show agreement with numerical results (symbols). This validates the analytical framework in § 3.3 for accurately predicting the UI and DI modulation under varying Atwood-number conditions.

A comparison between the processes of modulating RMI under total-transmission and non-total-transmission conditions (§§ 3.2 and 3.4) reveals that the presence of zero-order reverberating waves significantly complicates the development of an analytical dimensionless model for RMI manipulation in a layered system. The total-transmission condition enables the derivation of (3.16)–(3.17), which clearly identify the dimensionless parameters governing RMI modulation at a layer. In contrast, when reverberating waves are present, it becomes considerably more challenging to theoretically derive explicit dimensionless parameters that determine the possible regimes of multi-interface RMI manipulation. Nevertheless, the Atwood numbers of the two interfaces (A_1 and A_2)

https://doi.org/10.1017/jfm.2025.11064 Published online by Cambridge University Press

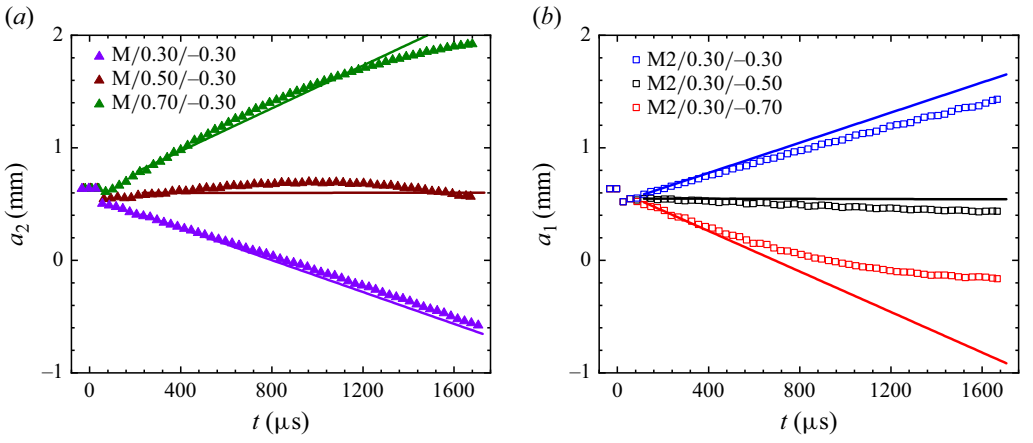


Figure 15. Comparison of the basic-mode amplitudes of the UI (a_1) and the DI (a_2) from simulations (symbols) with those predicted by models (lines) for the cases designed to manipulate RMI at the DI (*a*) and the cases aiming to control perturbation growth at the UI (*b*).

remain the key dimensionless parameters governing the modulation of multi-interface RMI, regardless of whether total-transmission conditions are met.

4. Conclusions

The Atwood-number dependence in a shock-accelerated heavy fluid layer is systematically examined through theoretical modelling and numerical simulations. To isolate the intrinsic interface-coupling effect, reverberating waves are eliminated by imposing a total-transmission condition at the DI. Variation of the UI Atwood number, A_1, reveals a strong influence on the morphological evolution of both interfaces. Specifically, an unexpected phase inversion is observed at the UI under low-A_1 conditions. As A_1 increases, the perturbation evolution at the DI progressively synchronizes in phase with that at the UI, indicating a strengthening of the UI-driven coupling. Phase inversion at the DI is absent under high-A_1 conditions. A comprehensive theoretical framework, incorporating startup, linear and nonlinear stages, is developed and validated to quantify the UI–DI coupling effect across a wide range of Atwood numbers.

Based on the established theory, we derive dimensionless formulae that define the modulation of multi-interface RMI under the total-transmission condition. Theoretical derivation first identifies four governing dimensionless parameters: the Atwood numbers of the UI and DI (A_1 and A_2), the dimensionless layer width, and the postshock amplitude ratio. The theory further proves that, in the absence of reverberating waves, it is theoretically impossible to simultaneously freeze perturbation growth at both interfaces by adjusting only the Atwood numbers. Eight distinct regimes of modulation achievable by varying A_1 and A_2 are identified and validated through numerical simulations. Moreover, the model applies to both in-phase and antiphase initial perturbations at the interfaces.

Subsequently, we systematically change both A_1 and A_2 to investigate the perturbation evolution in a shocked fluid layer with reverberating waves. The influence of A_1 on perturbation growth is found to be similar to that in scenarios without reverberations. When A_2 is increased while A_1 is held constant, the enhanced interface-coupling effect is counterbalanced by stronger rarefaction waves inside the layer. As a result, the amplitude growth rate at the UI remains largely insensitive to changes in A_2. In contrast, the growth of the DI amplitude shows a clear positive correlation with A_2. A theoretical model

https://doi.org/10.1017/jfm.2025.11064 Published online by Cambridge University Press

that incorporates both the interface-coupling effect and reverberating waves is derived, quantifying the dependence of linear perturbation growth on the Atwood numbers in a shocked heavy layer. Importantly, the results show that under high-A_2 conditions, accurate prediction of amplitude evolution at both the UI and DI requires the consideration of more than four reverberating waves within the layer.

Finally, we investigate the manipulation of instability in a shock-accelerated heavy layer with reverberating waves. Guided by the proposed theory, we strategically configure A_1 and A_2 to achieve targeted control over instability growth. This approach allows for the independent modulation of perturbation growth at the DI for a fixed A_2, and at the UI for a fixed A_1. Simulations confirm these theoretical predictions, successfully demonstrating distinct modulation scenarios at each interface. Crucially, this study establishes that instability growth at one interface can be controlled by adjusting the Atwood number of the opposite interface, irrespective of the presence of reverberating waves.

These findings enhance the fundamental understanding of instability manipulation in shocked fluid layers. Moreover, they suggest a potential application in ICF: by strategically choosing ablator materials to adjust the interface Atwood numbers inside the capsule, hydrodynamic instabilities during ignition could be effectively suppressed. While the current work concentrates on the interaction of a fluid layer with a weak shock, future studies will employ compressible theories to examine how modulation of instability depends on the Atwood number under strong shock conditions. The resulting compressible models for multi-interface RMI need to fully account for how acoustic waves, induced by shock–interface interactions, influence perturbation evolution. It should also be noted that the present investigation deals exclusively with perturbation growth at successive interfaces between gaseous media. Subsequent research will extend this analysis to include the effects of material properties such as elasticity and viscosity, with the goal of exploring instabilities at interfaces involving solid and liquid, conditions frequently encountered in ICF capsules.

Funding. This work was supported by the National Natural Science Foundation of China (nos. 123B2034, 12372281 and 12388101) and the Strategic Priority Research Program of Chinese Academy of Sciences (no. XDB0620201).

Declaration of interests. The authors report no conflict of interest.

References

Abarzhi, S.I., Bhowmick, A.K., Naveh, A., Pandian, A., Swisher, N.C., Stellingwerf, R.F. & Arnett, W.D. 2019 Supernova, nuclear synthesis, fluid instabilities, and interfacial mixing. *Proc. Natl Acad. Sci. USA* **116**, 18184–18192.

Abgrall, R. & Karni, S. 2001 Computations of compressible multifluids. *J. Comput. Phys.* **169**, 594–623.

Amendt, P. 2021 Entropy generation from hydrodynamic mixing in inertial confinement fusion indirect-drive targets. *Phys. Plasmas* **28**, 072701.

Bates, J.W. 2004 Initial-value-problem solution for isolated rippled shock fronts in arbitrary fluid media. *Phys. Rev. E* **69**, 056313.

Betti, R. & Hurricane, O.A. 2016 Inertial-confinement fusion with lasers. *Nat. Phys.* **12**, 435–448.

Billet, G. & Abgrall, R. 2003 An adaptive shock-capturing algorithm for solving unsteady reactive flows. *Comput. Fluids* **32**, 1473–1495.

Brouillette, M. 2002 The Richtmyer–Meshkov instability. *Annu. Rev. Fluid Mech.* **34**, 445–468.

Calvo-Rivera, A., Velikovich, A.L. & Huete, C. 2023 On the stability of piston-driven planar shocks. *J. Fluid Mech.* **964**, A33.

Cao, Q., Li, J., Wang, H., Zhai, Z. & Luo, X. 2024 Coupled Richtmyer–Meshkov and Kelvin–Helmholtz instability on a shock-accelerated inclined single-mode interface. *J. Fluid Mech.* **996**, A37.

Chen, C., Li, J., Wang, H., Zhai, Z. & Luo, X. 2025*a* Attenuation of Richtmyer–Meshkov instability growth of fluid layer via double shock. *Sci. China-Phys. Mech. Astron.* **68**, 244711.

https://doi.org/10.1017/jfm.2025.11064 Published online by Cambridge University Press

CHEN, C., LI, X., MA, Y., ZHAI, Z. & LUO, X. 2025*b* Modulation of the insta*b*ility growth at sequential heavy–light interfaces in a shocked dual layer. *J. Fluid Mech.* **1014**, A4.
CHEN, C., WANG, H., ZHAI, Z. & LUO, X. 2024 Mode coupling between two different interfaces of a gas layer subject to a shock. *J. Fluid Mech.* **984**, A38.
CHEN, C., XING, Y., WANG, H., ZHAI, Z. & LUO, X. 2023 Experimental study on Richtmyer–Meshkov instability at a light–heavy interface over a wide range of atwood numbers. *J. Fluid Mech.* **975**, A29.
COBOS CAMPOS, F. & WOUCHUK, J.G. 2016 Analytical scalings of the linear Richtmyer–Meshkov instability when a shock is reflected. *Phys. Rev. E* **93**, 053111.
COBOS-CAMPOS, F. & WOUCHUK, J.G. 2017 Analytical scalings of the linear Richtmyer–Meshkov instability when a rarefaction is reflected. *Phys. Rev. E* **96**, 013102.
COLLINS, B.D. & JACOBS, J.W. 2002 PLIF flow visualization and measurements of the Richtmyer–Meshkov instability of an air/SF_6 interface. *J. Fluid Mech.* **464**, 113–136.
CONG, Z., GUO, X., ZHOU, Z., CHENG, W. & SI, T. 2024 Freeze-out of perturbation growth for shocked heavy fluid layers by eliminating reverberating waves. *J. Fluid Mech.* **987**, A10.
DELL, Z., STELLINGWERF, R.F. & ABARZHI, S.I. 2015 Effect of initial perturbation amplitude on Richtmyer–Meshkov flows induced by strong shocks. *Phys. Plamas* **22**, 092711.
DIMONTE, G. & RAMAPRABHU, P. 2010 Simulations and model of the nonlinear Richtmyer–Meshkov instability. *Phys. Fluids* **22**, 014104.
DING, J., SI, T., CHEN, M., ZHAI, Z., LU, X. & LUO, X. 2017 On the interaction of a planar shock with a three-dimensional light gas cylinder. *J. Fluid Mech.* **828**, 289–317.
HAAN, S.W. 1991 Weakly nonlinear hydrodynamic instabilities in inertial fusion. *Phys. Fluids B* **3**, 2349–2355.
HAN, Z. & YIN, X. 1993 *Shock Dynamics*. Kluwer Academic Publisher.
HAWLEY, J.F. & ZABUSKY, N.J. 1989 Vortex paradigm for shock-accelerated density-stratified interfaces. *Phys. Rev. Lett.* **63**, 1241–1244.
JACOBS, J.W., JENKINS, D.G., KLEIN, D.L. & BENJAMIN, R.F. 1995 Nonlinear growth of the shock-accelerated instability of a thin fluid layer. *J. Fluid Mech.* **295**, 23–42.
JACOBS, J.W., KLEIN, D.L., JENKINS, D.G. & BENJAMIN, R.F. 1993 Instability growth patterns of a shock-accelerated thin fluid layer. *Phys. Rev. Lett.* **70**, 583–586.
JIANG, G. & SHU, C. 1996 Efficient implementation of weighted ENO schemes. *J. Comput. Phys.* **126**, 202–228.
KRITCHER, A.L., *et al.* 2022 Design of inertial fusion implosions reaching the burning plasma regime. *Nat. Phys.* **18**, 251–258.
LI, J., CAO, Q., WANG, H., ZHAI, Z. & LUO, X. 2023 New interface formation method for shock-interface interaction studies. *Exp. Fluids* **64**, 170.
LI, J., CHEN, C., ZHAI, Z. & LUO, X. 2024*a* Asymptotic matching modal model on Richtmyer–Meshkov instability. *J. Fluid Mech.* **1002**, A16.
LI, J., CHEN, C., ZHAI, Z. & LUO, X. 2024*b* Effects of compressi*b*ility on Richtmyer–Meshkov instability of heavy/light interface. *Phys. Fluids* **36**, 056104.
LIANG, Y. & LUO, X. 2023 Hydrodynamic instabilities of two successive slow/fast interfaces induced by a weak shock. *J. Fluid Mech.* **955**, A40.
LINDL, J., LANDEN, O., EDWARDS, J., MOSES, E. & TEAM, N. 2014 Review of the national ignition campaign 2009–2012. *Phys. Plasmas* **21**, 020501.
LOBATCHEV, V. & BETTI, R. 2000 Ablative stabilization of the deceleration phase Rayleigh–Taylor instability. *Phys. Rev. Lett.* **85**, 4522–4525.
LOMBARDINI, M., HILL, D.J., PULLIN, D.I. & MEIRON, D.I. 2011 Atwood ratio dependence of Richtmyer–Meshkov flows under reshock conditions using large-eddy simulations. *J. Fluid Mech.* **670**, 439–480.
LOMBARDINI, M. & PULLIN, D.I. 2009 Startup process in the Richtmyer–Meshkov instability. *Phys. Fluids* **21**, 044104.
MANSOOR, M.M., DALTON, S.M., MARTINEZ, A.A., DESJARDINS, T., CHARONKO, J.J. & PRESTRIDGE, K.P. 2020 The effect of initial conditions on mixing transition of the Richtmyer–Meshkov instability. *J. Fluid Mech.* **904**, A3.
MARIANI, C., VANDENBOOMGAERDE, M., JOURDAN, G., SOUFFLAND, D. & HOUAS, L. 2008 Investigation of the Richtmyer–Meshkov instability with stereolithographed interfaces. *Phys. Rev. Lett.* **100**, 254503.
MESHKOV, E.E. 1969 Instability of the interface of two gases accelerated by a shock wave. *Fluid Dyn.* **4**, 101–104.
MIKAELIAN, K.O. 1985 Richtmyer–Meshkov instabilities in stratified fluids. *Phys. Rev. A* **31**, 410–419.
MIKAELIAN, K.O. 1994 Freeze-out and the effect of compressibility in the Richtmyer–Meshkov instability. *Phys. Fluids* **6**, 356–368.

https://doi.org/10.1017/jfm.2025.11064 Published online by Cambridge University Press

MIKAELIAN, K.O. 1996 Numerical simulations of Richtmyer–Meshkov instabilities in finite-thickness fluid layers. *Phys. Fluids* **8**, 1269–1292.

MIKAELIAN, K.O. 2003 Explicit expressions for the evolution of single-mode Rayleigh–Taylor and Richtmyer–Meshkov instabilities at arbitrary Atwood numbers. *Phys. Rev. E* **67**, 026319.

MIKAELIAN, K.O. 2005 Rayleigh–Taylor and Richtmyer–Meshkov instabilities and mixing in stratified cylindrical shells. *Phys. Fluids* **17**, 094105.

MOTL, B., OAKLEY, J., RANJAN, D., WEBER, C., ANDERSON, M. & BONAZZA, R. 2009 Numerical investigation of the stability of a shock accelerated interface between two fluids. *Phys. Fluids* **21**, 126102.

NAPIERALSKI, M., COBOS, F., VELIKOVICH, A.L. & HUETE, C. 2024 Richtmyer–Meshkov instability when a shock is reflected for fluids with arbitrary equation of state. *J. Fluid Mech.* **1000**, A18.

NIEDERHAUS, C.E. & JACOBS, J.W. 2003 Experimental study of the Richtmyer–Meshkov instability of incompressible fluids. *J. Fluid Mech.* **485**, 243–277.

NISHIHARA, K., WOUCHUK, J.G., MATSUOKA, C., ISHIZAKI, R. & ZHAKHOVSKY, V.V. 2010 Richtmyer–Meshkov instability: theory of linear and nonlinear evolution. *Phil. Trans. R. Soc. A* **368**, 1769–1807.

QIAO, X. & LAN, K. 2021 Novel target designs to mitigate hydrodynamic instabilities growth in inertial confinement fusion. *Phys. Rev. Lett.* **126**, 185001.

RANJAN, D., OAKLEY, J. & BONAZZA, R. 2011 Shock-bubble interactions. *Annu. Rev. Fluid Mech.* **43**, 117–140.

RAVID, A., CITRON, R.I. & JEANLOZ, R. 2021 Hydrodynamic instability at impact interfaces and planetary implications. *Nat. Commun.* **12**, 2104.

RICHTMYER, R.D. 1960 Taylor instability in shock acceleration of compressible fluids. *Commun. Pure Appl. Math.* **13**, 297–319.

SADOT, O., EREZ, L., ALON, U., ORON, D., LEVIN, L.A., EREZ, G., BEN-DOR, G. & SHVARTS, D. 1998 Study of nonlinear evolution of single-mode and two-bubble interaction under Richtmyer–Meshkov instability. *Phys. Rev. Lett.* **80**, 1654–1657.

STERBENTZ, D.M., JEKEL, C.F., WHITE, D.A., AUBRY, S., LORENZANA, H.E. & BELOF, J.L. 2022 Design optimization for Richtmyer–Meshkov instability suppression at shock-compressed material interfaces. *Phys. Fluids* **34**, 082109.

THORNBER, B., DRIKAKIS, D., YOUNGS, D.L. & WILLIAMS, R.J.R. 2010 The influence of initial conditions on turbulent mixing due to Richtmyer–Meshkov instability. *J. Fluid Mech.* **654**, 99–139.

VANDENBOOMGAERDE, M., MÜGLER, C. & GAUTHIER, S. 1998 Impulsive model for the Richtmyer–Meshkov instability. *Phys. Rev. E* **58**, 1874–1882.

VANDENBOOMGAERDE, M., SOUFFLAND, D., MARIANI, C., BIAMINO, L., JOURDAN, G. & HOUAS, L. 2014 An experimental and numerical investigation of the dependency on the initial conditions of the Richtmyer–Meshkov instability. *Phys. Fluids* **26**, 024109.

VELIKOVICH, A.L., HERRMANN, M. & ABARZHI, S. 2014 Perturbation theory and numerical modelling of weakly and moderately nonlinear dynamics of the incompressible Richtmyer–Meshkov instability. *J. Fluid Mech.* **751**, 432–479.

VELIKOVICH, A.L. & PHILLIPS, L. 1996 Instability of a plane centered rarefaction wave. *Phys. Fluids* **8**, 1107–1118.

WOUCHUK, J.G. 2001*a* Growth rate of the linear Richtmyer–Meshkov instability when a rarefaction is reflected. *Phys. Plasmas* **8**, 2890–2907.

WOUCHUK, J.G. 2001*b* Growth rate of the linear Richtmyer–Meshkov insta*b*ility when a shock is reflected. *Phys. Rev. E* **63**, 056303.

WOUCHUK, J.G. & LÓPEZ CAVADA, J. 2004 Spontaneous acoustic emission of a corrugated shock wave in the presence of a reflecting surface. *Phys. Rev. E* **70**, 046303.

WOUCHUK, J.G. & NISHIHARA, K. 1996 Linear perturbation growth at a shocked interface. *Phys. Plasmas* **3**, 3761–3776.

WOUCHUK, J.G. & NISHIHARA, K. 1997 Asymptotic growth in the linear Richtmyer–Meshkov instability. *Phys. Plasmas* **4**, 1028–1038.

XING, Y., CHEN, C., LI, J., WANG, H., ZHAI, Z. & LUO, X. 2025 Atwood-number dependence of the Richtmyer–Meshkov instability at a heavy–light single-mode interface. *J. Fluid Mech.* **1007**, A54.

YANG, Y., ZHANG, Q. & SHARP, DH. 1994 Small amplitude theory of Richtmyer–Meshkov instability. *Phys. Fluids* **6**, 1856–1873.

YUAN, M., ZHAO, Z., LIU, L., WANG, P., LIU, N. & LU, X. 2024 Instability evolution on a shock-accelerated cylindrical fluid layer with arbitrary Atwood numbers. *J. Fluid Mech.* **1000**, A9.

ZABUSKY, N.J. 1999 Vortex paradigm for accelerated inhomogeneous flows: visiometrics for the Rayleigh–Taylor and Richtmyer–Meshkov environments. *Annu. Rev. Fluid Mech.* **31**, 495–536.

https://doi.org/10.1017/jfm.2025.11064 Published online by Cambridge University Press

ZHAI, Z., CHEN, C., XING, Y., LI, J., CAO, Q., WANG, H. & LUO, X. 2025 Manipulation of Richtmyer–Meshkov instability on a heavy-light interface via successive shocks. *J. Fluid Mech.* **1003**, A9.

ZHANG, Q. & GUO, W. 2016 Universality of finger growth in two-dimensional Rayleigh–Taylor and Richtmyer–Meshkov instabilities with all density ratios. *J. Fluid Mech.* **786**, 47–61.

ZHANG, Q. & GUO, W. 2022 Quantitative theory for spikes and bubbles in the Richtmyer–Meshkov instability at arbitrary density ratios. *Phys. Rev. Fluids* **7**, 093904.

ZHANG, Q. & SOHN, S.I. 1997 Nonlinear theory of unstable fluid mixing driven by shock wave. *Phys. Fluids* **9**, 1106–1124.

ZHOU, N., ZHAI, Z. & LUO, X. 2025*a* Manipulation on *a* heavy fluid layer with dual-mode perturbations via reverberating waves. *Phys. Rev. Fluids* **10**, 023904.

ZHOU, Y. 2017*a* Rayleigh-Taylor and Richtmyer–Meshkov instability induced flow, turbulence, and mixing. I. *Phys. Rep* **720–722**, 1–136.

ZHOU, Y. 2017*b* Rayleigh–Taylor and Richtmyer–Meshkov insta*b*ility induced flow, turbulence, and mixing. II. *Phys. Rep* **723–725**, 1–160.

ZHOU, Y. 2024 *Hydrodynamic Instabilities and Turbulence: Rayleigh–Taylor, Richtmyer-Meshkov, and Kelvin–Helmholtz Mixing*. Cambridge University Press.

ZHOU, Y., SADLER, J.D. & HURRICANE, O.A. 2025*b* Instabilities and mixing in inertial confinement fusion. *Annu. Rev. Fluid Mech.* **57**, 197–225.

ZHOU, Y., *et al.* 2021 Rayleigh–Taylor and Richtmyer–Meshkov instabilities: a journey through scales. *Phys. D* **423**, 132838.

ZYLSTRA, A.B. 2022 Burning plasma achieved in inertial fusion. *Nature* **601**, 542–548.

https://doi.org/10.1017/jfm.2025.11064 Published online by Cambridge University Press